NATÁLIA SILVA

Investigating hydroclimate changes in Antarctica during 1900-2014

São Paulo

2022

NATÁLIA SILVA

Investigating hydroclimate changes in Antarctica during 1900-2014

Master's thesis submitted to the Oceanographic Institute of the University of São Paulo as partial fulfillment of the requirements for the degree of Master of Science in Oceanography, with emphasis on Physical Oceanography.

Advisor: Dr. Ilana E. K. C. Wainer

São Paulo

2022

SILVA, Natália. **Investigating hydroclimate changes in Antarctica during 1900-2014.**. Master's thesis submitted to the Oceanographic Institute of the University of Sao Paulo as partial fulfillment of the requirements for the degree of Master of Science in Oceanography, with emphasis on Physical Oceanography.

Evaluated on ____ / ____ / _____

Judging Committee

Prof PhD _____ Institution _____

Grade _____ Signature _____

Prof PhD _____ Institution _____

Grade _____ Signature _____

Prof PhD _____ Institution _____

Grade _____ Signature _____

Agradecimentos

Esse projeto não poderia ter sido desenvolvido sem um rol de pessoas que me apoiaram profissional- e pessoalmente durante um período sombrio de pandemia. Agradeço:

À minha orientadora Ilana, com quem desenvolvi esse projeto em conjunto. Por todas as ideias, comentários, correções e incentivos; e por se fazer presente mesmo em dois anos à distância no *home office*.

Aos colegas de OC2 – Blanka, Bruno, Eduardo, Fernanda, Gabriel, Ivana, Iuri, Laura, Lucas, Luciana, Marcos, Marina, Paulo e Pedro – com quem pude compartilhar ideias, problemas, dificuldades e soluções. Certamente essa dissertação contou com a contribuição de todos vocês.

A todos os docentes e profissionais com os quais pude aprender ao longo da minha – ainda breve – carreira, e aos que me possibilitaram oportunidades de aprender, ganhar experiência e melhorar.

Aos meus amigos nos mais diferentes núcleos – e aqui tomo a licença de omitir nomes, pois definitivamente esqueceria alguns: os "da ilha", os da "época de escola", os da "faculdade", os "do 65/2", os "da hamburgueria", os "do muay thai", os "do funcional", os "do crossfit", os "da natação"... Obrigada, amigos <3

À minha psicóloga Maísa, que me ajuda a navegar pela vida sempre repetindo seu mantra *"Faça o que de ti depende; de resto deja firme e tranquila".*

Nos dois anos que compreenderam meu período de mestrado, uma pandemia acontecia no mundo. Se chegamos até aqui, agora, foi graças aos cientistas, profissionais da saúde, profissionais de serviços essenciais e não-negacionistas. Obrigada por cuidarem da nossa vida.

Final- e principalmente, agradeço à minha família – mamãe, papai, Gugu, José, Lu, vó, Maju e João. Nada existe para mim sem vocês.

Esse projeto foi financiado pelo Conselho Nacional de Desenvolvimento Científico e Tecnológico, processo número 130290/2020-3.

"If Antarctica were music, it would be Mozart. Art, and it would be Michelangelo. Literature, and it would be Shakespeare. And yet it is something even greater; the only place on earth that is still as it should be.

May we never tame it."

– Andrew Denton

RESUMO

SILVA, Natália. **Investigando mudanças no hidrocima da Antártica entre 1900-2014**. 2022. Dissertação (Mestrado) - Instituto Oceanográfico, Universidade de São Paulo, São Paulo.

O hidroclima da região Austral influencia o Manto de Gelo Antártico (AIS, de *Antarctic Ice Sheet*) e, por consequência, o clima global. No AIS, a precipitação (PPT) está diretamente relacionada com o balanço de massa na superfície, e tem aumentado nos últimos séculos como resposta ao aquecimento global. Em particular, o aumento da PPT se intensificou nas últimas décadas, quando o clima passou a ser determinado pelas atividades humanas ao invés de variabilidade natural. Usando 23 modelos do CMIP6 e sete reanálises, encontramos mudanças na precipitação considerando os períodos antes (1900–1979) e depois (1980–2014) do ano de 1980. Com a média das multi-reanálises, estimamos tendências de PPT de 8.2e-3 e 1.3e-2 mm dia^{-1} década^{-1} durante 1900–1979 e 1980–2014, respectivamente, para a média da região Austral (ao sul de 60° S). Por sua vez, a média do conjunto de modelos captou uma aceleração de sete vezes nas tendências de PPT desde o período "antes de 1980" até o período "depois de 1980" (2.1e-3 a 1.5e-2 mm dia^{-1} década^{-1}). Entretanto, as mudanças de PPT não foram espacialmente homogêneas. Enquanto a precipitação aumentou na área ao sul de 60° S em média, a porção oeste do continente e o Mar de Ross tornaram-se mais secos. Também analisamos a temperatura da superfície do mar do Oceano Austral e a circulação atmosférica, dois principais moduladores da chuva na Antártica. Consistentes com estudos anteriores, nossos resultados mostraram que a precipitação na Antártica durante 1900–2014 foi determinada principalmente pela dinâmica atmosférica, em oposição à influência termodinâmica da superfície do oceano.

Palavras-chave: Antártica, precipitação, balanço de massa, mudanças climáticas, CMIP6

ABSTRACT

SILVA, Natália. **Investigating hydroclimate changes in Antarctica during 1900-2014**. 2022. Master's Dissertation - Oceanographic Institute, University of Sao Paulo, Sao Paulo.

The hydroclimate of high southern latitudes impacts the Antarctic Ice Sheet (AIS) and, by consequence, the global climate. Precipitation (PPT) is directly related to the surface mass balance in the AIS and has increased over the past centuries as a response to global warming. In particular, the upward PPT trend accelerated in the late 20th Century, when anthropogenic forcing overcame natural variability in determining the climate. Using twenty-three CMIP6 models and seven reanalyses, we found PPT changes considering the periods before (1900-1979) and after (1980-2014) the year 1980. In the averaged Austral region, PPT trends for the multi-reanalyses mean grew 60% from the previous period to the contemporary: from 8.2e-3 to 1.3e-2 mm day^{-1} decade^{-1} for 1900-1979 and 1980-2014, respectively; The multi-model mean captured a sevenfold acceleration in PPT trends from the "before 1980" to the "after 1980" period (2.1e-3 to 1.5e-2 mm day^{-1} decade^{-1}). However, PPT changes were spatially heterogeneous. While a general rainfall increase occurred south of 60° S, the western-West AIS and the Ross Sea regions became drier. We also analyzed the Southern Ocean's sea surface temperature and atmospheric circulation, two principal modulators of Antarctic rainfall. Consistent with previous studies, we found that PPT in Antarctica throughout 1900-2014 was primarily determined by atmospheric dynamics rather than the thermodynamical influence of the ocean surface.

Key-words: Antarctica, precipitation, mass balance, climate change, CMIP6

List of Figures

List of Tables

Acronyms

AIS	Antarctic Ice Sheet
AMIP	CMIP6 AMIP experiment 23 multi-model mean
ABS	Amundsen-Bellingshausen Sea
AP	Antarctic Peninsula
ASL	Amundsen Sea Low
CMIP6	Coupled Model Intercomparison Project Phase 6
DJF	Southern Hemisphere summer (December, January, and February)
EAIS	East Antarctic Ice Sheet
JJA	Southern Hemisphere winter (June, July, and August)
MAM	Southern Hemisphere fall (March, April and May)
MMM23	CMIP6 Historical experiment 23 multi-model mean
MRM7	7 multi-reanalysis mean
PPT	precipitation rate
r	Pearson correlation coefficient
RMSD	centered root-mean-square difference
SAM	Southern Annular Mode
SMB	surface mass balance
SLP	sea level pressure
SO	Southern Ocean
SON	Southern Hemisphere spring (September, October, November)
SST	sea surface temperature
STD	standard deviation
TD	Taylor diagram
V-wnd	meridional component of wind at the 500hPa level
WAIS	West Antarctic Ice Sheet
ZW3	Zonal Wave Three

Contents

1 Introduction

The Antarctic Ice Sheet (AIS) accounts for about 88% of the total ice mass and 70% of all freshwater on Earth (Allison et al., 2009), plus it retains 58 meters of potential sea-level rise (Slater et al., 2020). Because of its significant contribution to sea-level change, the role played by AIS in a changing climate scenario is of regional and global concern (Velicogna & Wahr, 2006; Shepherd et al., 2012; Dalaiden et al., 2019; IPCC, 2021). The amount of fresh and cold water locked from or released to the ocean and the high albedo of ice surfaces are principal AIS mechanisms to modulate the climate system (Eisen et al., 2008); It affects the water cycle, the radiation budget, the atmospheric circulation, and the Meridional Overturning Circulation (Hanna et al., 2013). Hence, any mass variation in the AIS may lead to changes in global climate (Clark et al., 1999; Thomas et al., 2017).

The Surface Mass Balance (SMB) is an important aspect of ice sheets, defined as the difference between the build-up of snow accumulation and its reduction due to sublimation, evaporation, wind erosion, wind-driven transport, melting, and calving (Shepherd et al., 2012; Van Wessem et al., 2014). The scheme from Zwally et al. (2015), in Figure 1.1, exhibits the processes that contribute to SMB and their interaction. Over the Antarctic Ice Sheet, most of these terms are small enough to be neglected, except for snow accumulation that corresponds to 91% of the total mass budget (Van de Berg et al., 2005; Roberts et al., 2014; Zwally et al., 2015; Van Wessem et al., 2018). Consequently, many studies address the AIS SMB based on precipitation (PPT), as discussed by Nicolas & Bromwich (2011b), Thomas et al. (2017), Van Wessem et al. (2018), and Medley & Thomas (2019).

Precipitation in Antarctica shows high temporal and spatial variability (Fyke et al., 2017), being naturally regulated by polar climate dynamics and teleconnections with low-latitude processes (Marshall, 2003; Schneider et al., 2015; Li et al., 2021). Other than natural variability, studies such as Lenaerts et al. (2018) link ozone depletion and increasing greenhouse gas (GHG) concentrations since 1970 with changes in the Antarctic

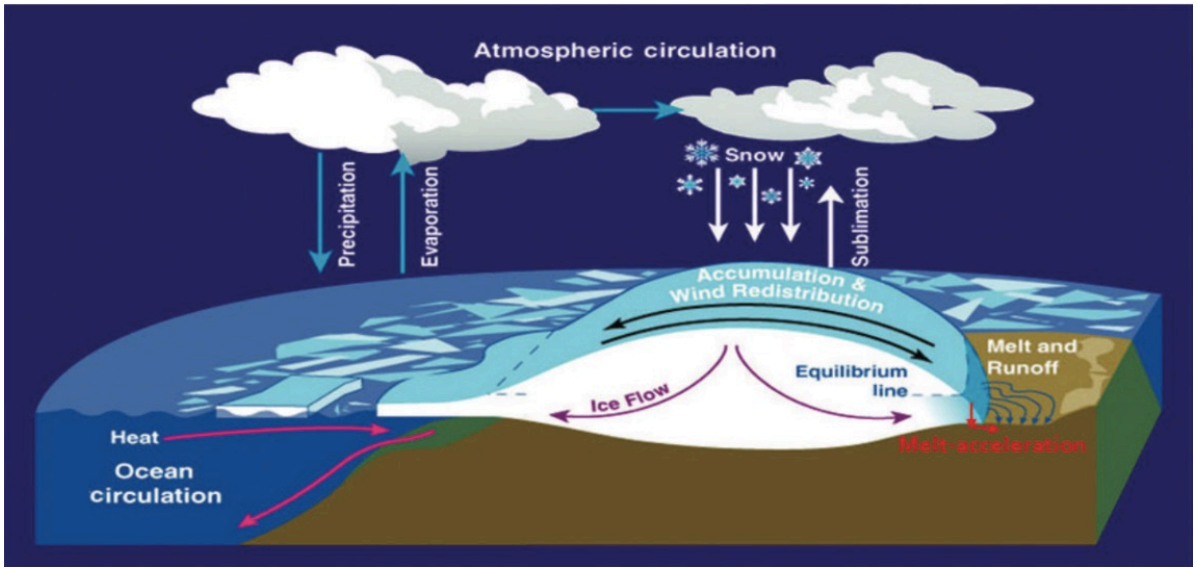

Figure 1.1: Principal processes that affect surface mass balance. Mass input from liquid and snow precipitation is the main component of SMB in the Antarctic Ice Sheet. From Zwally et al. (2015).

climate, including rainfall. However, the effect of anthropogenically forced signals on PPT is still in debate (Thomas et al., 2017; IPCC, 2021).

IPCC (2021) discusses that around the world, on average, PPT has increased and will continue to do so in response to global warming. Particularly, Antarctica seems to be a region that tends to experience enhanced rainfall as a function of climate change. Figure 1.2, retrieved from IPCC (2021), quantifies how much PPT in Antarctica is expected to vary according to simulated global warming thresholds.

Bromwich et al. (2011) calculated a PPT increase within 1 to 26 mm from 1989 to 2009 over Antarctica and the Southern Ocean (SO). Goodwin et al. (2003) and Thomas et al. (2015) estimated a 30% rise in snow accumulation, respectively, in East AIS (EAIS) during 1960-1985 and West AIS (WAIS) during 1979-2009. A doubling in snow accumulation over the Antarctic Peninsula (AP) from 1850 to 2006 appeared in the results of Thomas et al. (2008). Moreover, the positive PPT trends have accelerated since 1979 (Wille et al., 2021; Medley & Thomas, 2019). For instance, over the averaged AIS, Medley & Thomas (2019) rated snow accumulation trends of 0.4 and 1 Gt year^{-2} between 1801-2000 and 1957-2000, respectively.

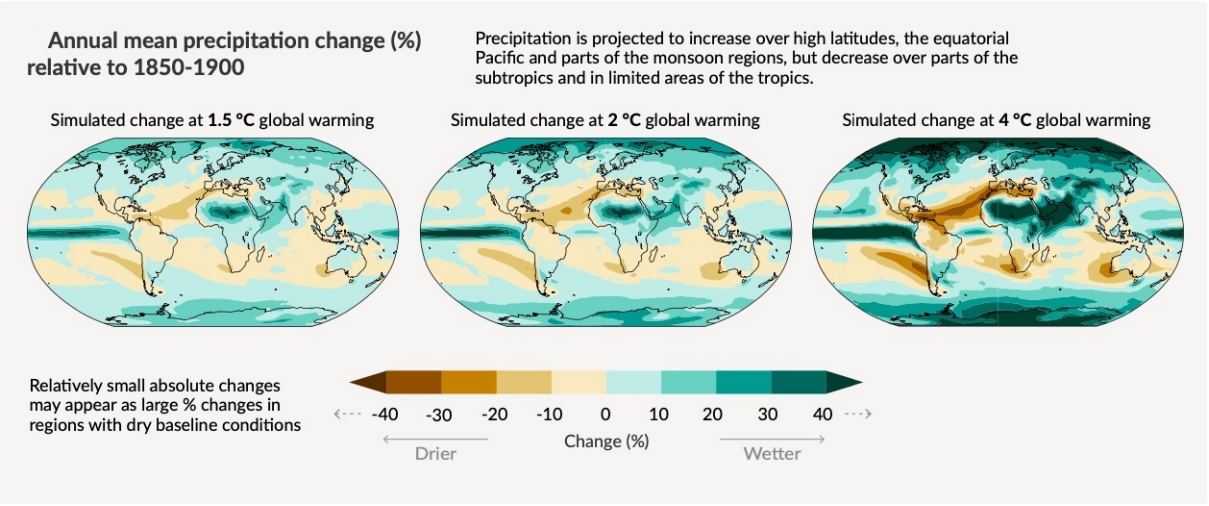

Figure 1.2: Expected precipitation change relative to 1850-1900, as a function of global warming thresholds (1.5° C on the left, 2° C in the center, and 4° C on the right). From IPCC (2021).

It is certain that a general rainfall increase has occurred south of 60° S since 1800 (Bracegirdle et al., 2019; IPCC, 2021). Yet, several studies highlight substantial regional differences in precipitation changes across Antarctica: as pointed by Wang et al. (2017) and IPCC (2021), the western-WAIS and the Antarctic Plateau experienced drier or unchanged conditions between 1900-2010.

The Southern Ocean (SO; ocean south of 60° S) is the primary source of moisture for PPT in Antarctica, hence essential for the AIS mass balance (Bromwich et al., 2011). According to Trenberth (2011), any slight variation in the sea surface temperature (SST) could cause profound changes in PPT, given that their spatial pattern and temporal evolution are strongly connected (Trenberth et al., 2005). Kittel et al. (2018) ran a sensibility test using a regional climate model and found that per each degree of SO warming, the AIS SMB should increase from 2% to 6%. Also, Yu et al. (2018) showed that between 2003-2018, 80% of PPT gains in Progress Station (69° S, 76 °E) happened because of enhanced total column of water vapor over the Indian Ocean Sector of the SO.

Contrary to global ocean warming, the SO's surface has been cooling since the decade of 1970 (Jones et al., 2016; Swart et al., 2018; Zhang et al., 2019; Doddridge et al., 2019). As stated in Purich et al. (2016), changes in the atmospheric circulation, driven by ozone

depletion and GHG concentration increase, have intensified the westerly jet; It, in turn, enhances the Ekman transport of cold coastal Antarctic waters northwards, resulting in negative SST trends. Another theory explaining such SST changes is cooling due to SO's surface freshening, which increases stratification and reduces convective mixing with warmer waters from the subsurface (Purich et al., 2018; Auger et al., 2021). Armour et al. (2016), for example, estimated trends of -0.2 °C decade^{-1} during 1982-2012 in the SO, except over the Amundsen Sea.

The SO's surface cooling is accompanied by sea ice increase (Donat-Magnin et al., 2020). Ice covering the ocean's surface diminishes the moisture exchange with the atmosphere, thus affecting PPT (Bracegirdle et al., 2019). However, addressing sea ice and its relationship with precipitation lies beyond the scope of this study.

Despite SST thermodynamically controlling PPT in the Austral region, their variations do not occur at the same pace. That is because the atmospheric circulation is also a key modulator of rainfall, determining to which regions moisture is advected (Nicolas & Bromwich, 2011b; Zwally et al., 2015; Philippe et al., 2016; Medley & Thomas, 2019; Rodehacke et al., 2020). The Antarctic coastline experiences the highest precipitation rates of the whole continent due to lying near the moisture source and because of the persistent cyclonic activity that advects humid air masses to this region (Goodwin et al., 2016; Schlosser et al., 2016). In the desert inland of Antarctica, the rare incursion of maritime air masses allows few annual PPT events (Philippe et al., 2016; Thomas et al., 2015).

Notably, the meridional flow is responsible for moisture exchange between mid-latitudes and Antarctica (Bromwich et al., 2011); When stronger, it provokes extreme precipitation events like those described by Emanuelsson et al. (2018) and Turner et al. (2019). The results of Nicolas & Bromwich (2011b) show that during 1989-2009, regions in Antarctica that experienced downward trends in meridional winds (enhanced southward flow) were associated with increased PPT.

High southern latitudes climate modes of variability are key to understanding changes in the Austral atmospheric circulation. The Zonal Wave 3 (ZW3) – third mode of vari-

ability in high southern latitudes – refers to meridional asymmetries in the zonally symmetric circulation along the latitudinal band 50°-60° S (Raphael, 2004). The ZW3 determines preferred regions of meridional flow that guides moisture transport into and out of Antarctica (Schlosser et al., 2018). Raphael (2004) defined an index based on the wave's amplitude to quantify its polarity, where a positive (negative) phase relates to a strong meridional (zonal) flow. The results found by Marshall et al. (2017) show that the effects of the ZW3 on PPT are more pronounced on the western side of Antarctica. When the ZW3 is in its positive polarity, an anticyclonic circulation centered at 150° W establishes offshore WAIS (Figure 1.3-A), creating a see-saw pattern of PPT anomalies, with more rainfall in the Antarctic Peninsula, the Weddell Sea, and Wilkes Land and less over the Ross Sea and western-WAIS (Figure 1.3-B). The ZW3's positive phase also enhances PPT in the Enderby Land, according to Marshall et al. (2017), as presented in Figure 1.3-B.

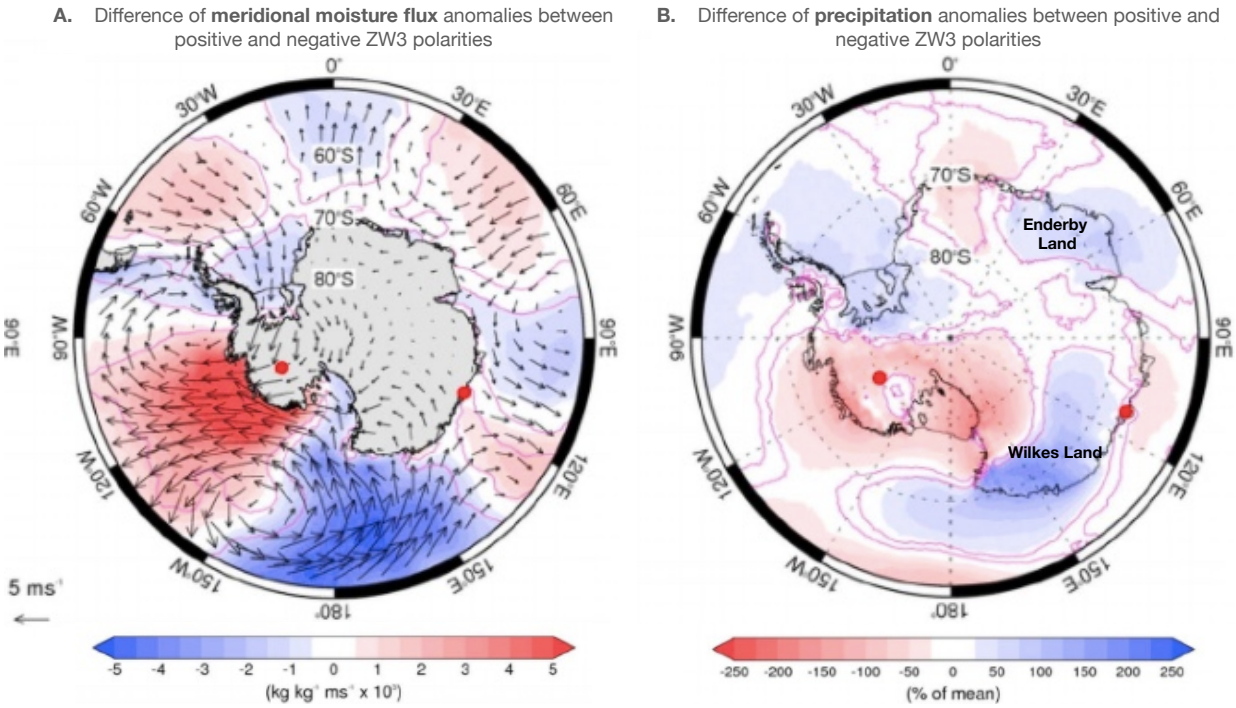

Figure 1.3: Anomalies in (A) meridional moisture flux and (B) precipitation related to the ZW3 positive polarity. Adapted from Marshall et al. (2017).

Besides the ZW3, the Southern Annular Mode (SAM) affects PPT in Antarctica. The SAM is the first mode of climate variability in high southern latitudes, driving over 30%

of the Austral climate (Thompson & Wallace, 2000; Marshall, 2007). This phenomenon represents a zonally symmetric ring-like structure around Antarctica, approximately on the latitudinal band of 60° S, and is determined by the pressure gradient between mid and high latitudes (Thompson & Wallace, 2000; Marshall, 2003). The index developed by Gong & Wang (1999) characterizes the positive (negative) polarity of the SAM as when the westerly trough is strengthened (weakened) and displaced poleward (equatorward). Countless studies have discussed the SAM shifting to a more positive polarity throughout the 20th century (Turner et al., 2005; Marshall, 2007; Purich et al., 2016; Marshall et al., 2017; Medley & Thomas, 2019). Particularly, IPCC (2021) discusses that human activity was responsible for high positive trends of the SAM index between 1970-1990.

Marshall et al. (2017) show that an intensified westerly jet transports moisture northwards, away from Antarctica. For this reason, the SAM's positive phase relates to drier conditions over most of EAIS (Marshall et al., 2017; Medley & Thomas, 2019). In the Antarctic Peninsula, where orography is the dominant mechanism for PPT, stronger westerly winds result in more rainfall (Bozkurt et al., 2021; Wille et al., 2021). Yu et al. (2018) presents the link between a positive SAM and increased cyclonic activity in Dronning Maud Land, Wilkes Land, and Marie Byrd Land, smb which enhances meridional moisture transport and causes more PPT over those areas. Between 1800-2000, Medley & Thomas (2019) found that atmospheric circulation was the dominant mechanism inducing Antarctic PPT; Specifically, they showed that 80% of its changes during 1957–2000 occurred due to positive SAM trends.

Given the global relevance of the Antarctic Ice Sheet, it is fundamental to understand one of its principal aspects, the surface mass balance. Hence, in this study, we investigate changes in PPT, the main component of the AIS SMB, throughout 1900-2014. We further aim to characterize which conditions drove the changes during this period. For that, we look at both thermodynamical and dynamical modulators of the high southern latitude climate, respectively, SST and the atmospheric circulation. Our epoch of interest (1900-2014), named Historical, covers a transitional period of climate; It goes back to a time when the climate evolved following natural variability at the beginning of the industrial

era, spanning to the present anthropogenically influenced state.

1.1 Hypothesis

As the IPCC (2021) suggests that PPT in Antarctica would increase because of global warming, we hypothesize that variations in the Southern Ocean surface temperature has changed precipitation from the beginning of the industrial era into the 21st Century.

1.2 Objectives

We aim to investigate how the precipitation changed in the Austral region during 1900-2014. Beyond that, we intend to verify if such changes are linked to variations in the Southern Ocean's sea surface temperature (SST) and atmospheric circulation. To test our hypothesis, we follow the specific goals:

i Validate the most contemporary numeric simulations in the Coupled Model Intercomparison Project by comparing them with reanalysis products;

ii Characterize the mean-field and changes in precipitation and SST throughout 1900-2014;

iii Verify whether the thermodynamical (SST) or the dynamical (circulation) condition was the main modulator to precipitation.

2 Data and Methods

In order to address the hypothesis and objectives described earlier, the following data and methods will be used.

2.1 Data

Observational data in Antarctica is sparse and irregular (Behrangi et al., 2016). Hence, to ensure complete spatial and temporal coverage, here we use reanalysis results and model simulations.

2.1.1 Reanalysis Datasets

Reanalysis products enable to fill in the gaps of observational data by merging and assimilating them into numerical models (Dee & Uppala, 2008; Sun et al., 2018). These products have the advantage of providing temporally continuous and spatially complete outputs.

The use of reanalysis is broad in austral climate studies (Nicolas & Bromwich, 2011a; Thomas et al. 2015; Marshall et al., 2017; Emanuelsson et al. 2018). As discussed in previous researches (as in Bromwich et al., 2011 or Medley & Thomas, 2019), the reanalyses are more accurate in representing the climate from 1979 onwards, over the "satellite era". Nevertheless, in addition to the contemporary reanalysis, we also used two 20th century products that extend back to 1836 (20Cv3) and 1900 (Era20C).

2.1.1.1 20Cv3

Here we use the third generation of the NOAA-CIRES-DOE Twentieth Century Reanalysis (20Cv3), which is globally distributed in a 1° x 1° horizontal resolution, spanning 1836-2015 (Slivinski et al., 2019). The model NCEP GFS v14.0.1 assimilates ISPD ver-

sion 4.7 observations of pressure, and HadISST2 SST and sea ice distributions are used as boundary conditions (Slivinski et al., 2019). According to Poli (2017), among the 20th century reanalyses available, 20Cv3 is more accurate in representing the high southern latitudes. 20th Century Reanalysis V3 data is provided by the NOAA/OAR/ESRL PSL, Boulder, Colorado, USA, from their Web site at `https://psl.noaa.gov/data/gridded/data.20thC_ReanV3.html` (last access on January 17, 2022).

2.1.1.2 CFSR

The National Centers for Environmental Prediction Climate Forecast System Reanalysis (CFSR) is a global reanalysis available from 1979 to 2011. It is generated by a coupled atmosphere-ocean-land surface-sea ice system that assimilates observed variations in CO2, aerosols, and solar variations (Saha et al., 2010). As reported by NCAR Staff Online (2017), CFSR is superior to other NCEP products. It has an improved and coupled model, better assimilation schemes, and is anchored on modern satellite observations (NCAR Staff Online, 2017). CFSR is available in several horizontal resolutions, from which we chose the 0.5° x 0.5° grid. CFSR data may be retrieved from the NCAR Research Data Archive, available on `https://rda.ucar.edu/datasets/ds093.1/` (last access on January 17, 2022).

2.1.1.3 Era20C

The ECMWF's atmospheric reanalysis of the 20th century (Era20C) spans from 1900 to 2010 (Poli et al., 2016). Surface observations of pressure and marine winds (from ISPDv3.2.6 and ICOADSv2.5.1) are assimilated into a coupled model (Poli, 2017). From the horizontal resolutions available, we selected 1° x 1°. Poli et al. (2016) note that after 1979, Era20C presents some problems. Era20C is available on the ECMWF portal on `https://apps.ecmwf.int/datasets/data/era20c-daily/levtype=sfc/type=an/` (last access on January 17, 2022).

2.1.1.4 EraInt

ECMWF Interim Re-Analysis (EraInt) is one of the most modern reanalyses of the institute (Simmons, 2006). It is a global atmospheric reanalysis available from 1979 to 2019. Here, we analyzed the 1° x 1° horizontal resolution. A key limitation of EraInt is the stronger water cycling over the ocean, which may impact the PPT output (Dick, 2019). Still, EraInt has been reported to produce a realistic representation of the climate on high southern latitudes regarding the PPT (Bromwich et al., 2011; Behrangi et al., 2016; Medley & Thomas, 2019). Monthly means of daily means for EraInt may be obtained the ECMWF portal on `https://apps.ecmwf.int/datasets/data/interim-full-daily/levtype=sfc/` (last access on January 17, 2022).

2.1.1.5 JRA55

55-year Reanalysis (JRA55) is the newest Japanese Meteorological Agency product (Kobayashi et al., 2015). We analyzed the JRA55 data in a 1.25° x 1.25° horizontal grid, from 1979 to 2011. JRA55 data may be retrieved from the NCAR Research Data Archive, available on `https://rda.ucar.edu/datasets/ds628.1/` (last access on January 17, 2022).

2.1.1.6 MERRA2

In this study, we also included the NASA Global Modeling and Assimilation Office's product Modern-Era Retrospective analysis for Research and Applications, version 2 (MERRA2), spanning from 1980-present. It is a global reanalysis that differs from others by incorporating cryospheric processes and trace gas constituents (Bosilovich et al., 2019). A key strength for MERRA2 is the improved estimate on SMB and temperature over ice sheets. Yet, over the oceans, the reanalysis overestimates the PPT rate (Bosilovich et al., 2015). Observations are the primary forcing source for PPT in MERRA2 from low latitudes to 62.5°. But due to the lack of gauge observations, PPT is entirely modeled on land surfaces south of 62.5° (Bosilovich et al., 2019). MERRA2 outputs are available at

the GES DISC portal, on https://disc.gsfc.nasa.gov/datasets?project=MERRA-2 (last access on January 17, 2022), in a 0.5 ° x 0.667 ° horizontal resolution.

2.1.1.7 NCEP2

The National Centers for Environmental Prediction (NCEP)/U.S. Department of Energy Atmospheric Model Intercomparison Project 2 reanalysis (NCEP2) is an upgraded version, with new observation data included and an improved model parametrization and assimilation (Kanamitsu et al., 2002). The NCEP2 is globally available for the 1979-2021 period in a 2.5°x 2.5° horizontal grid, which is the coarsest resolution analyzed in this work. NCEP Reanalysis 2 data provided by the NOAA/OAR/ESRL PSL, Boulder, Colorado, USA, from their Web site at https://psl.noaa.gov/data/gridded/data.ncep.reanalysis2.html (last access on January 17, 2022).

We interpolated all reanalyses in a 1° x 1° horizontal resolution and only analyzed data within 1900-2014. Not all of them overlap before 1980 and after 2010. Plus, by calculating the arithmetic mean at each grid point and time among the datasets, we obtained their ensemble mean, hereafter named MRM7.

Table 2.1 below summarizes major information on each reanalysis product used in this study.

Table 2.1: Reanalyses information.

Label	Reanalysis	Institution	Time range	Grid	Reference
a	20Cv3	NOAA	1836-2015	1° x 1°	Slivinski et al. (2019)
b	CFSR	NCEP	1979-2011	2.5° x 2.5°	Saha et al. (2010)
c	Era20C	ECMWF	1900-2010	1° x 1°	Poli et al. (2016)
d	EraInt	ECMWF	1979-2019	1° x 1°	Simmons (2006)
e	JRA55	JMA	1979-2011	1.25° x 1.25°	Kobayashi et al. (2015)
f	MERRA2	NASA	1980-2021	0.5 ° x 0.667 °	Bosilovich et al. (2015)
g	NCEP2	NCEP	1979-2021	2.5° x 2.5°	Kanamitsu et al. (2002)
	MRM7		**1900-2014**	**1° x 1°**	

2.1.2 CMIP6 Simulations

Along with the reanalysis products, we included simulations outputs from a set of 23 models of the Coupled Model Intercomparison Project Phase 6 (CMIP6; Eyring et al., 2016) in our investigation. They are displayed in Table 2.2.

Table 2.2: CMIP6 models included in this study.

Label	Model	Institution	Reference
A	ACCESS-ESM1-5	CSIRO, Australia	Ziehn et al. (2020)
B	BCC-ESM1	BCC, China	Wu et al. (2020)
C	CAMS-CSM1-0	CAMS, China	Rong et al. (2018)
D	CanESM5	CCCma, Canada	Swart et al. (2019)
E	CESM2	NCAR, USA	Lauritzen et al. (2018)
F	CMCC-CM2-HR4	CMCC, Italy	Cherchi et al. (2019)
G	CNRM-CM6-1	CNRM-CERFACS, France	Voldoire et al. (2019)
H	E3SM-1-0	DOE, USA	Golaz et al. (2019)
I	EC-Earth3-Veg	EC-Earth-Consortium, Sweden	Wyser et al. (2020)
J	FGOALS-g3	CAS, China	Li et al. (2020)
K	FIO-ESM-2-0	FIO, China	Bao et al. (2020)
L	GISS-E2-1-G	NASA-GISS, USA	Kelley et al. (2020)
M	HadGEM3-GC31-LL	MOHC, UK	Roberts et al. (2014)
N	IITM-ESM	IITM, India	Krishnan et al. (2021)
O	INM-CM5-0	INM, Russia	Volodin et al. (2019)
P	IPSL-CM6A-LR	IPSL, France	Lurton et al. (2020)
Q	MIROC-ES2L	MIROC, Japan	Hajima et al. (2020)
R	MPI-ESM1-2-LR	MPI, Germany	Mauritsen et al. (2019)
S	MRI-ESM2-0	MRI, Japan	Yukimoto et al. (2019)
T	NESM	NUIST, China	Cao et al. (2018)
U	NorESM2-LM	NCC, Norway	Seland et al. (2020)
V	TaiESM1	RCEC, Taiwan	Wang et al. (2021b)
W	UKESM1-0-LL	MOHC, UK	Sellar et al. (2019)

The 23 models that submitted data to the Earth System Grid Federation (ESGF) by the time we started this project were analyzed (Table 2.2). The data is available on `https://esgf-node.llnl.gov/`. Each center uses distinct methods to develop a model that represents the climate system. When we use a multi-model approach, it becomes possible to evaluate the climate through various perspectives, enabling a more representative idea of the reality (Ferrero et al., 2021).

In this study, we are interested in addressing the climate evolution from a time when it was driven mostly by natural-forcing agents (i.e., orbital parameters, solar irradiance, stratospheric aerosols of volcanic origin, and greenhouse gas concentrations) to the current anthropogenic-forced state Jungclaus et al. (2017). In this sense, an assemblage of scientific studies found that the late 20th century (around the decade 1980) was the climate's turning point when human activity overcame natural variability (Goodwin et al., 2016; Lenaerts et al., 2018; Dalaiden et al., 2019; Medley & Thomas, 2019). To cover this transitional period, we have chosen to access the Historical experiment within the CMIP6 project, that considers the years from 1850 to 2014.

To allow comparison with the Reanalyses, we evaluated the period common for both (1900-2014) and interpolated all the models to a 1° x 1° horizontal resolution. At last, by calculating the arithmetic mean among the models at each grid point and time, we obtained the models' ensemble mean, hereafter MMM23.

For the same 23 models (Table 2.2), we examined simulations results from the Atmospheric Model Intercomparison Project (AMIP; Eyring et al., 2016) to conduct a secondary analysis. In the AMIP configuration, observations of SST and sea ice are used as prescribed boundary conditions (Roussel et al., 2020). This configuration enables us to try and separate the deep-ocean dynamics role on forcing the climate (Taylor et al., 2012). AMIP data is available on `https://esgf-node.llnl.gov/` from 1979 to 2014. To investigate whether the oceanic or atmospheric dynamic was dominant in forcing the climate after 1979, we compared the outputs from MRM7, MMM23, and the 23 models' AMIP ensemble mean (hereafter AMIP). According to Roussel et al. (2020), the coupled models are highly biased on SST, implying that the AMIP-simulated PPT is more akin to observations.

2.1.3 Variables of interest

We addressed the following variables to investigate the Austral hydroclimate and the mechanisms responsible for its changes: precipitation rate (PPT) and sea surface temperature (SST) for both Reanalysis and models; and sea level pressure (SLP), and the

meridional wind component at the 500hPa level (V-wnd) solely for reanalysis.

2.2 Methods

After interpolating all datasets to a 1° x 1° horizontal grid, we conducted all of our analyses south of 40° S.

For PPT, it was necessary to standardize units among the datasets to obtain all in mm day^{-1}. Table 2.3 displays the original PPT unit for each dataset (reanalyses and models) and the means used to convert them. Some of the SST data was originally in Kelvin; To standardize all in degrees Celsius, we subtracted those by 273.15.

Table 2.3: Methods to standardize PPT units in mm day $^{-1}$.

Datasets	Original unit	Conversion to mm day^{-1} method
20Cv3 CFSR MERRA2 NCEP2 All CMIP6 models	mm s^{-1}	PPT × 86400
Era20C EraInt	m month $^{-1}$	PPT × 1000 ÷ 30
JRA55 **MRM7** **CMIP6**	mm day^{-1}	-

As mentioned in section 2.1.2, we focus on comparing the climate before and after a transitional period around the decades 1970-1980. Lenaerts et al. (2018) discuss that after 1970, the climate in Antarctica has been driven by changes in the atmospheric circulation due to the ozone hole; For instance, Monaghan et al. (2006) and Thomas et al. (2015) show relevant PPT trends in Antarctica after 1979. Therefore, we carried our analysis by separating the data into two periods: spanning from 1900-1979 and 1980-2014, hereafter referred to as "before 1980 (B1980)" and "after 80 (A1980)", respectively.

2.2.1 Regional approach

Substantial evidence points that PPT trends in Antarctica vary regionally; For instance, rainfall has increased in the Antarctic Peninsula, whereas Victoria Land has become drier (Nicolas & Bromwich, 2011a; Frieler et al., 2015 Thomas et al., 2017; Medley & Thomas, 2019). To understand which parts of Antarctica contribute to changes on a continental-wide scale is important to address the climate from a regional approach.

Motivated to find regional differences, we split Antarctica into five regions (Figure 2.1), each with distinct climate regimes:

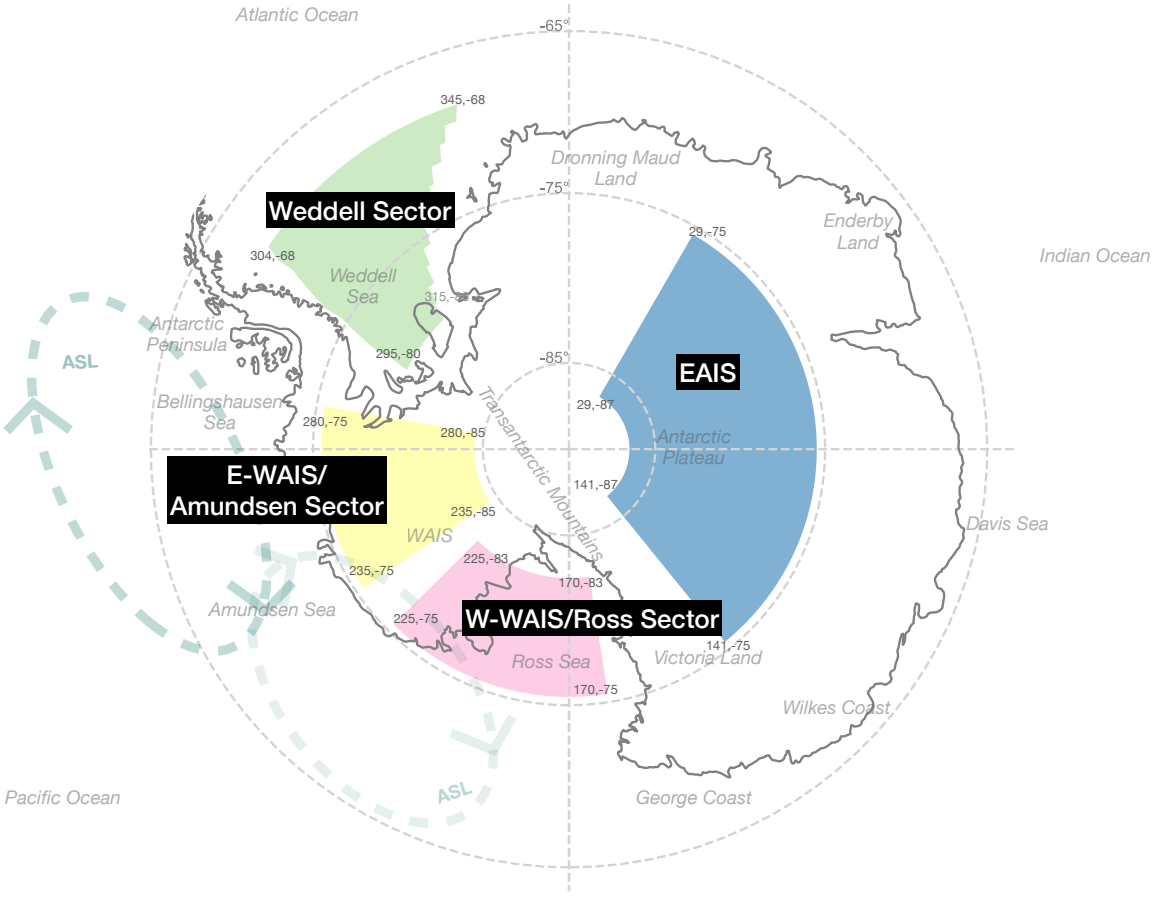

Figure 2.1: Colored areas show regions of interest in Antarctica (EAIS, W-WAIS/Ross Sector, E-WAIS/Amundsen Sector, and Weddell Sector). Antarctic regions referred to along the text are named on the map.

– **Austral**, which comprehends everything poleward of 60° S.

– East Antarctica Ice Sheet (**EAIS**), an entirely continental region on the Antarctic plateau bounded by the coordinates 29° - 141° E and 75° - 87° S. EAIS presents low precipitation rates due to its long distance from the oceanic moisture source and cold temperatures (Krinner et al., 2007). Besides, only a few snow events occur in this region during a year, contributing to more than 50% of the annual accumulation (Thomas et al., 2017). Other than those snow events, EAIS experiences PPT that occurs when the air in the atmosphere is almost saturated and is further cooled by mixing with the colder air of the inversion layer or by radiative processes (Stenni et al., 2017). There is a strong positive correlation linking the PPT in the EAIS with the ZW3, for when its index is positive more moisture is advected to the plateau. As for the SAM index, the opposite is true; When it is negative, more meridional flow is allowed, and the PPT intensifies (Thomas et al., 2017).

– Eastern-West Antarctica and the Amundsen Sea Sector (**E-WAIS/Amundsen Sector**) is situated between WAIS and the southern Antarctic Peninsula (AP) on low-elevation terrains, which allows moist air masses to penetrate inland (Nicolas & Bromwich, 2011a). The coordinates 125° - 80° W and 75° - 85° S limit this region. According to Thomas et al. (2015), the Amundsen Sea Low (ASL) is the dominant mechanism for PPT in E-WAIS/Amundsen Sector. Its cyclonic rotation creates moisture advection paths into the region (see scheme in Figure 1). The ASL longitudinal shifts determine preferred areas of northerly flow (Wille et al., 2021); when its eastern flank places over the Amundsen Sea, the humidity transport enhances in E-WAIS/Amundsen Sector (Donat-Magnin et al., 2020). Given the ASL deepening (Raphael et al., 2016) and migration north-eastwards (Turner et al., 2013), PPT in E-WAIS/Amundsen Sector has been observed to grow, especially during the late 20th century (Thomas et al., 2008; Thomas et al., 2015).

– Western-West Antarctica and the Ross Sea Sector (**W-WAIS/Ross Sector**) lies within 170° E - 135° W and 75° - 83° S. The katabatic winds that flow from the Transantarctic Mountains to the Ross Sea block moisture penetration to Antarc-

tica, causing this region to be relatively dry (Turner et al., 2019). It is also a geographically diverse region: to the west lies a low-lying ice shelf exposed to the ocean, whereas to the east, there is the steep relief of the Transantarctic Mountains (Thomas et al., 2017; Emanuelsson et al., 2018; Turner et al., 2019). Like occurs in the easternmost WAIS region, the strength and position of the ASL determines the frequency and trajectory of storms in the Ross Sea; When it is weak, anticyclones penetrate the Ross Sea and advect moisture into W-WAIS/Ross Sector (Raphael et al., 2016; Emanuelsson et al., 2018). In fact, Thomas et al. (2017) found that between 1950-2010, W-WAIS/Ross Sector underwent a notable decrease in snow accumulation.

– Weddell Sea Sector (**Weddell Sector**) is the ocean-only region eastward of the AP. This region is encompassed by the polygon with vertices on (56° W, 68°S), (15° W, 68°S), (45° W, 80° S), and (65° W, 80° S). As the Weddell Sector lies on the eastern side of the AP, it is affected by the warm and dry air that descends from the mountains. Due to such a relationship between orography, winds, and PPT (named the Foehn effect), this already dry region may experience even lower precipitation rates on account of the westerlies' strengthening (Bozkurt et al., 2021). Thomas et al. (2017) suggest that the Weddell Sector has a positive correlation with the ASL and with sea ice concentration over the Weddell and Bellingshausen seas. Furthermore, those authors discuss that anticyclonic activity over the Weddell Sea could draw northerly moist air masses into the region.

2.2.2 Taylor Diagram

We used Taylor Diagrams in an effort to validate the climate models and identify how close they match observations. Taylor Diagrams offer a graphical summary of the models' reliability based on their statistical proximity with a reference value (Taylor, 2005), which we assume here as the reanalyses ensemble mean (MRM7). Their correlation, centered root-mean-square difference (RMSD), and the standard deviations (STD) are evaluated

(Taylor, 2001). We analyzed simulated PPT and SST for the 23 CMIP6 models and compared them with MRM7. The more alike the amplitude of variation (i.e., STD), smaller RMSD, and stronger correlation with the reference value, the more realistic the model is supposed to be.

2.2.3 Statistics

We calculated trends through the linear least-squares regression method and their statistical significance using a two-sided Wald Test (Gourieroux et al., 1982). For a large sample size, the Wald test is a t-test equivalent (Agresti, 1990). We defined three thresholds for the statistical significance of our analyzes: p-value > 0.1 (over 10% chance of trends happening by chance), p-value < 0.05, and p-value < 0.01 (less than 5% and 1% chance of trends happening by chance, respectively). Through the least-square fit, we obtained the R-squared values as well.

To addressing correlations among variables, we used the Pearson correlation coefficient (r; Lee Rodgers & Nicewander, 1988).

2.2.4 Multi-model approach and Model Agreement

No matter how elaborated the models are, it is fundamentally impossible to describe all the complex processes involved in the climate system (Tebaldi & Knutti, 2007).

The ideal method to obtain the closest match to reality and reduce the datasets uncertainties is a multi-model approach, as the products complement each other (Tebaldi & Knutti, 2007; Ferrero et al., 2021). The combination of many datasets has demonstrated to increase the reliability of the analysis in diverse areas of expertise, for instance, in climate, technologies, public health, or agriculture (Tebaldi & Knutti, 2007).

The ensemble size necessary to reduce the noise of internal variability, and focus on the datasets' response to external forcing, depends on the region, period, and the variable of interest (Milinski et al., 2020; Maher et al., 2021). Here, we addressed seven reanalyses and 23 global climate models.

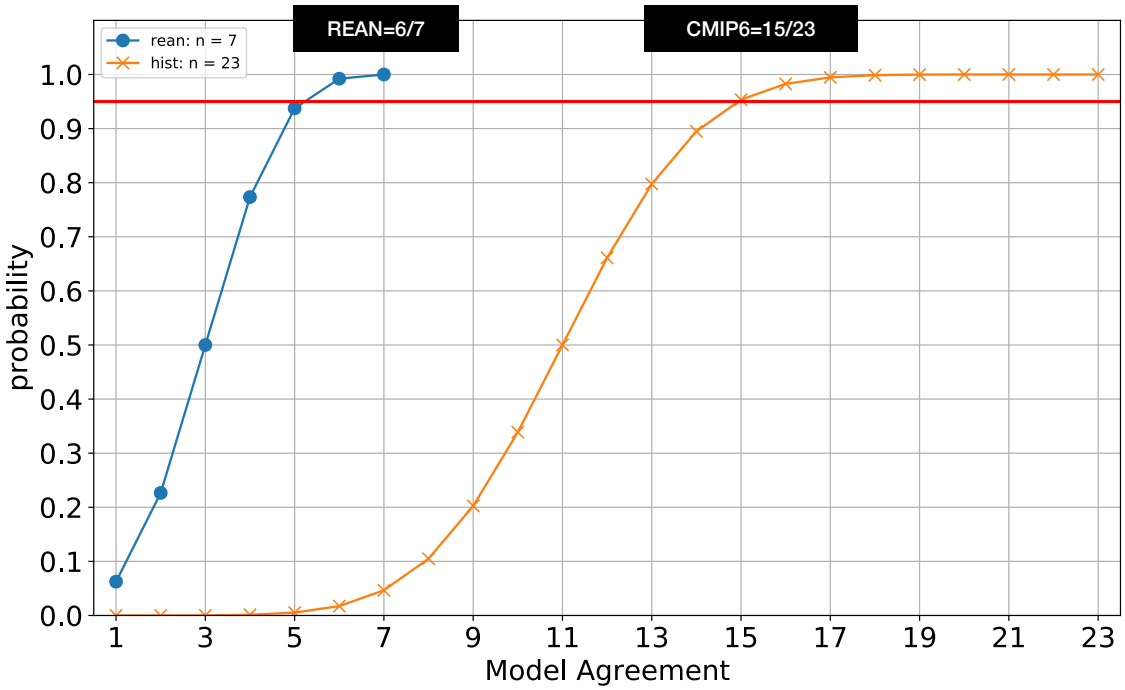

Figure 2.2: CDF for binomial distributions with p = q = 0.5, as in Pontes et al. (2020), for N = 7 (reanalyses) and N = 23 (models).

We estimated the statistical significance of our "multi-datasets" analyses through model agreement, using the Robust Rank Test (Fligner & Policello, 1981; for methodological details, see Pontes et al., 2020). Figure 2.2 shows the cumulative distribution function (CDF) for N = 7 (reanalyses), and N = 23 (models). For our multi-datasets analysis results to achieve a significance level of 95%, 6 out of 7 Reanalysis products (≈ 86%) and 15 out of 23 model simulations (≈ 65%) must agree.

2.2.5 SAM and ZW3 indices

It has been shown that atmospheric circulation is a primary driver for PPT in high southern latitudes, pushing moist air masses into the Austral region (Nicolas & Bromwich, 2011a; Marshall et al., 2017). We address the atmospheric influences on PPT through two of the most important patterns of large-scale variability for the Southern Hemisphere: the Southern Annular Mode (SAM) and the Zonal Wave Three (ZW3).

We calculated the SAM and ZW3 indices (hereafter I_{SAM} and I_{ZW3}) following the

protocols from Gong & Wang (1999) and Raphael (2004), respectively. I_{SAM} is based on the SLP difference between the zonal mean of 40° S and 65° S. In equation 2.1, P* is the SLP normalized by the standard deviation.

$$I_{SAM} = P*_{40S} - P*_{65S} \tag{2.1}$$

Raphael (2004) defines the I_{ZW3} according to equation 2.2. This index indicates the average state of SLP at the wave's ridges – specifically, at the grid points 50° E, 166° E, and 76° W, all in 49° S; Hence, the three-values average in equation 2.2. Also, $SLP_{seasonal}$ represents the three-monthly – or seasonal – SLP value, $\overline{SLP_{seasonal}}$ is the 1900-2014 climatological seasonal value, and $\sigma_{seasonal}$, the seasonal standard deviation.

$$I_{ZW3} = \frac{1}{3}\sum_{i=1}^{3}\frac{(SLP_{seasonal} - \overline{SLP_{seasonal}})}{\sigma_{seasonal}} \tag{2.2}$$

2.2.6 Code availability

All Python codes created to perform our analyses are available on `https://github.com/snatalias/Precipitation_changes_in_Antarctica.git`.

3 Results and Discussion

3.1 Model validation

Initially, we show the models' ability in representing PPT and SST (Figure 3.1, see labels in Table 2.2). For PPT (Figure 3.1-A), most models had correlations values with MRM7 within the range 0.5-0.8; The highest value (0.79) occurred between MRM7 and the multi-model mean (MMM23). The average RMSD was 0.02, with MMM23 being the lowest. with respect to the STD, models #A, #O, #S, and MMM23 agree with MRM7; Models #Q and #U showed lower STD, and all others presented higher STD values.

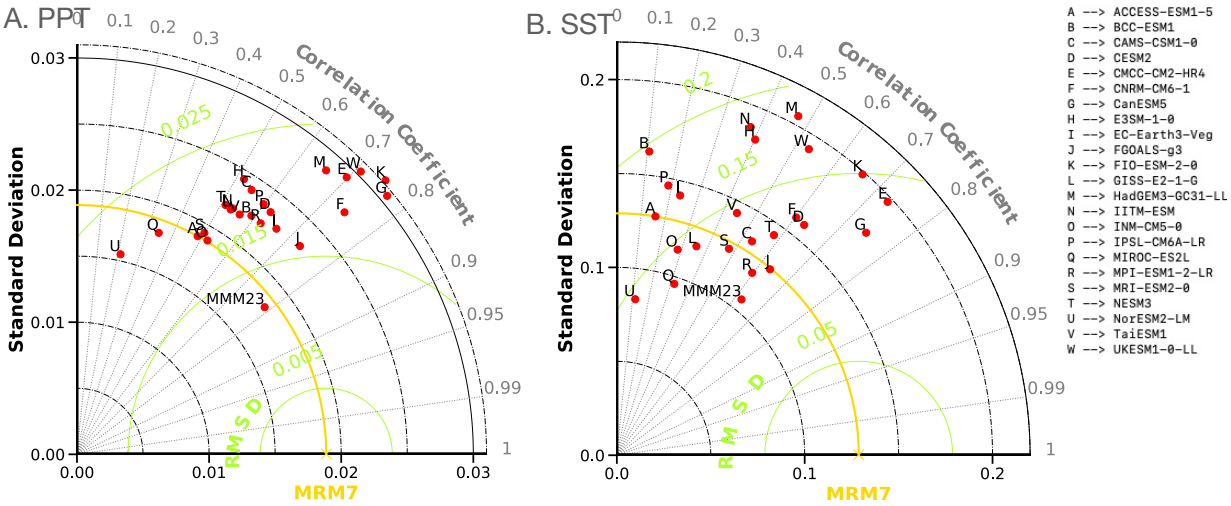

Figure 3.1: Taylor Diagrams for (A) precipitation and (B) sea surface temperature. The 23 models are labeled as in Table 2.2. The reference value is the multi-reanalysis mean (MRM7). MMM23 represents the multi-model mean.

The simulated SST showed a large spread between the products (Figure 3.1-B). The correlation coefficients varied in a broad range, from 0.1 (models #B and #U) to 0.74 (model #G); #G, #E, #K had stronger correlations with MRM7. STD varied from 0.08 to 0.2 (reference value = 0.13), suggesting diverse amplitude of variation between products. Models #A, #J, and #S had closer STD to MRM7. The multi-model mean

(MMM23) had the lowest RMSD, while models #B, #H, #N, and #M had the highest values.

The Taylor diagrams confirmed the expected – as discussed in section 2.2.4 – regarding the potential of the multi-model mean on masking structural differences and reducing uncertainties of single products (Tebaldi & Knutti, 2007; Semenov & Stratonovitch, 2010). When considering the three statistics results (r, STD, and RMSD), MMM23 was closer to MRM7 than individual simulations, suggesting that it is the best representation of reality in our analysis.

3.2 Precipitation poleward of 40° S

3.2.1 1900-2014 mean precipitation rates

Figure 3.2 shows the mean-field of precipitation poleward of 40° S from 1900 to 2014 for reanalysis products. Their spatial pattern is consistent with Behrangi et al. (2016).

All reanalyses showed that in the interior of Antarctica – on the plateau – precipitation rates were slightly above zero (< 0.5 mm day^{-1}). In the Wilkes Coast (location in Figure 2.1), where storms from the Indian Ocean often arrive (Thomas et al., 2017), high PPT appeared. In coastal WAIS and the Southern Ocean (SO), PPT was 2-3 mm day^{-1}, and varied from 3 to 5 mm day^{-1} over the ocean north of 60° S.

Rainfall in the Weddell and Ross seas was up to 1 mm day^{-1}, but the reanalyses differed in the region extension. For instance, the low PPT (< 1 mm day^{-1}) over the Weddell Sea reached 62° S in Era20C and hardly extended to 69° S in CFSR.

The reanalyses reproduced the orographic effect on rainfall (Foehn effect) over the Andes' windward side, where PPT reached 16 mm day^{-1}. Such phenomenon was expected in the mountainous Antarctic Peninsula as well (Bozkurt et al., 2021); all reanalyses but Era20C and NCEP2 were able to reproduce it.

Regarding the reanalysis agreement on the mean-field on PPT, at least 6 out of 7 products lay within the 2 STD interval ($MRM7\ mean \pm 1STD$) in the Antarctic plateau, the interior of WAIS, and the Brazil-Malvinas Confluence (around 45-50° S and 50-70°

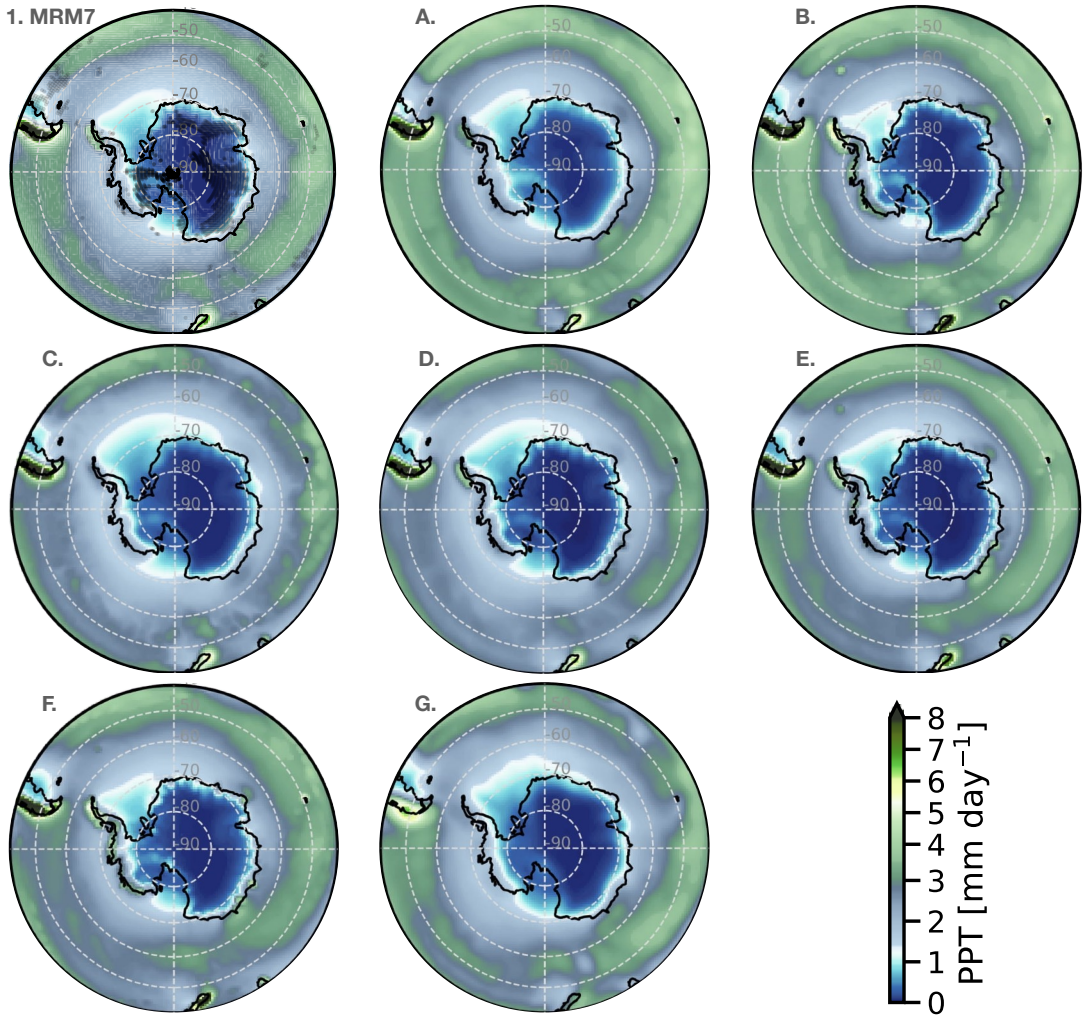

Figure 3.2: Mean-field of precipitation rates, in mm day^{-1}, during 1900-2014. The panels show PPT for (1) the multi-reanalysis mean (MRM7) and (A-G) individual products labeled as in Table 2.1. Stippling on MRM7 indicates the dataset's agreement at the 95% significance level within the interval $MRM7\ mean \pm 1STD$ ($\approx$ 86% agreement).

W in Figure 3.2-1); they exceeded such range in the Antarctic seas and over the ocean.

The reanalysis products were consistent in reproducing PPT inland Antarctica, whereas some differences appeared over the ocean (Appendix-A): NCEP2 (-8%) and the ECMWF's products (-13%) were drier compared to MRM7, while 20Cv3 (+12%) and CFSR (+15%) had higher PPT. Compared to MRM7, JRA55 and MERRA had more (+12%) PPT in the SO opposite to fewer (-8%) over the ocean north of 60° S. Studies that focus on reanalysis products performance discuss that since 1979 EraInt is more consistent with

observations (Bromwich et al., 2011; Behrangi et al., 2016; Palerme et al., 2017a).

The spatial pattern of PPT south of 40°S simulated by CMIP6 models was consistent with the reanalyses (Figure 3.3) and with Behrangi et al. (2016). As implied from the stippling in Figure 3.3-1, the datasets agreed within the 2 STD interval (*MMM23 mean* $\pm$ $1STD$) in the entire region; a few grid points over the ocean, particularly in the Amundsen-Bellingshausen Sea (ABS), were exceptions.

Precipitation rates in the Weddell and Ross seas and Antarctica varied within 0-1.5 mm day^{-1}. In comparison to MRM7, the multi-model mean (MMM23) simulated a smaller region of low PPT ($<$ 1 mm day^{-1}) over the Weddell Sea (Figures 3.2-1 and 3.3-1). The models combined (MMM23) were able to reproduce the orographic effect on PPT in southern South America but not in the AP. In the SO, PPT ranged between 1.5-3 mm day^{-1}, with a regional peak on the Wilkes coast ($\approx$4 mm day^{-1}). North of 60° S, the rainfall rates were 3-5 mm day^{-1}. These results agree with MRM7.

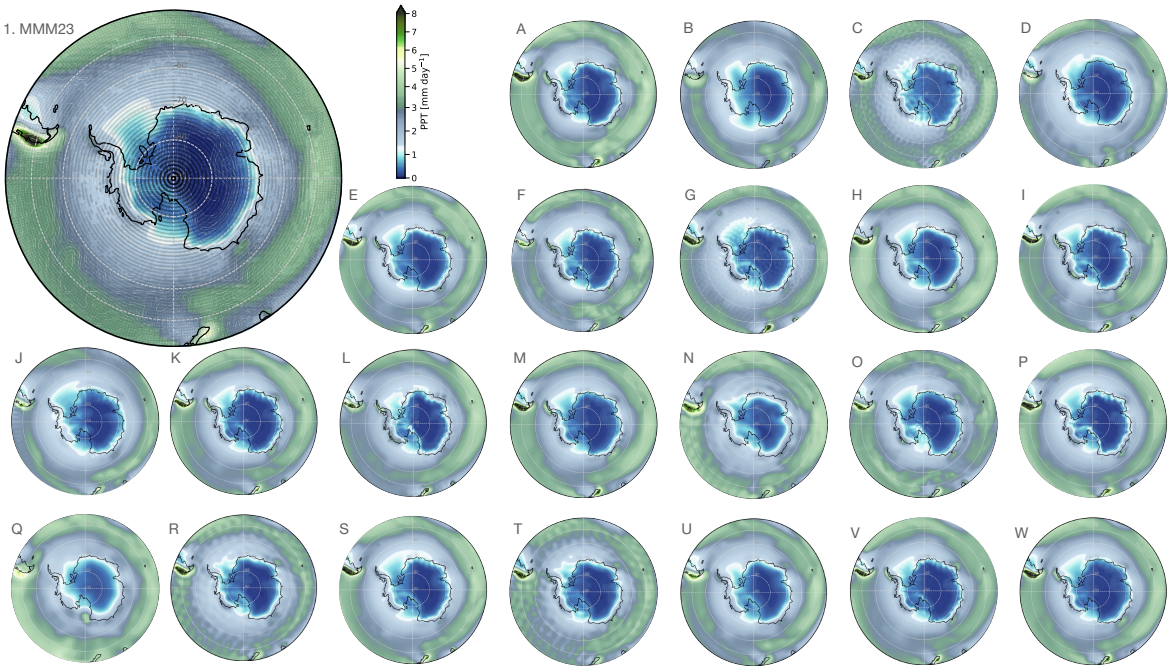

Figure 3.3: Mean-field of precipitation rates, in mm day^{-1}, during 1900-2014. The panels show PPT for (1) the multi-model mean (MMM23) and (A-W) individual products labeled as in Table 2.2. Stippling on MMM23 indicates model agreement at the 95% significance level within the interval *MMM23 mean* $\pm$ $1STD$ ($\approx$ 65% agreement).

3.2.2 Seasonal cycle

For the reanalyses, a moderate seasonal cycle throughout 1900-2014 appeared in the Austral region (Figure 3.4-A), with slightly larger PPT (+0.2 mm day $^{-1}$) in fall (March-May; MAM). Behrangi et al. (2016) also found that poleward of 60° S, fall was the most humid season.

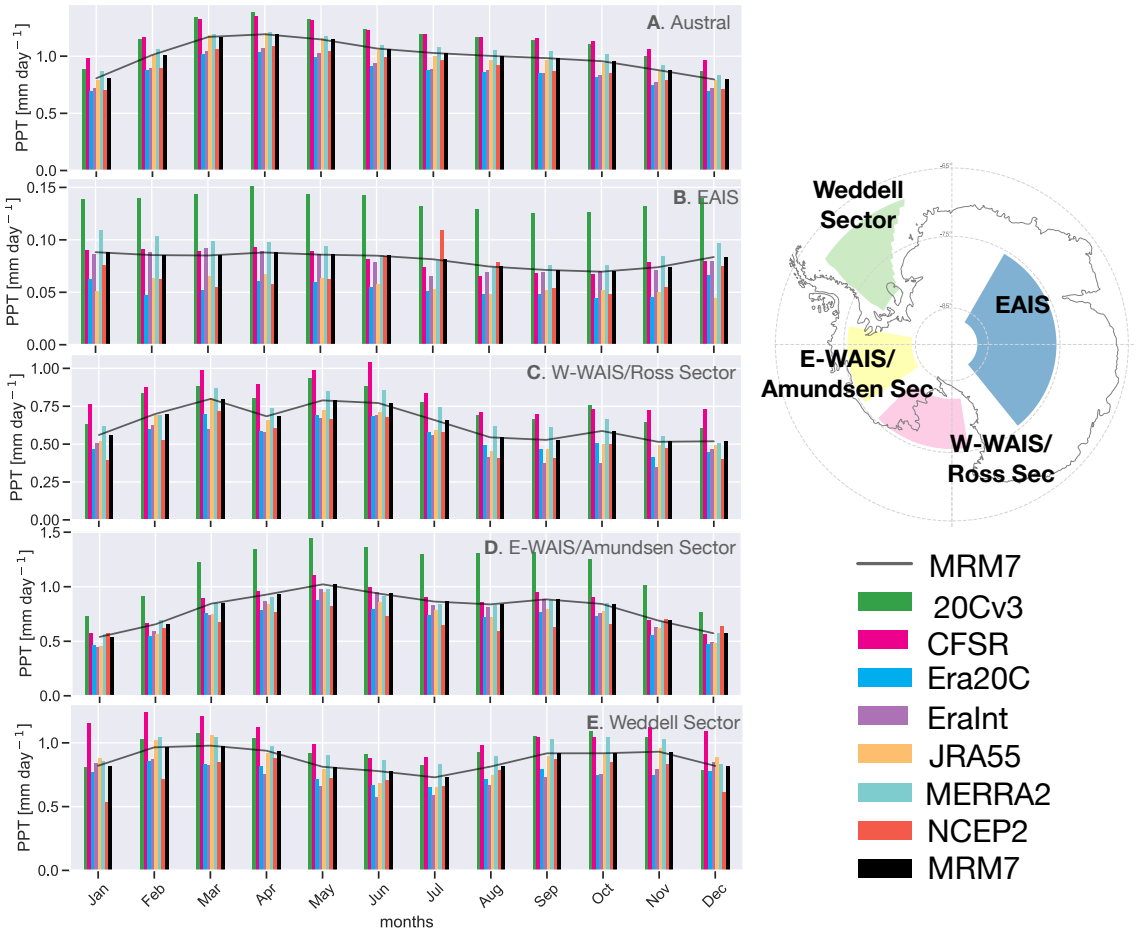

Figure 3.4: Climatological 1900-2014 seasonal cycle of PPT, in mm day^{-1}. Panels A-E represent Antarctic regions, as indicated by the map on the label. The bars correspond to individual reanalysis, and the solid line refers to the ensemble mean (MRM7). Note the different y-axis scales on each panel.

In EAIS (Figure 3.4-B), the seasonal cycle was even more subtle owing to its high elevation and geographic location. Roussel et al. (2020) discusses that over the plateau, minimum PPT occur during spring (September-November; SON), which appears in Fig-

ure 3.4-B as a 20% rainfall drop.

The three other regions that are alongside the ocean show marked seasonality for PPT. In W-WAIS/Ross Sector (Figure 3.4-C), the average rainfall rate during spring and summer (December-February; DJF) was 0.5 mm day $^{-1}$; it was 0.75 mm day $^{-1}$ in fall and winter (June-August; JJA). The E-WAIS/Amundsen Sector (Figure 3.4-D) was wetter from April to September, as PPT nearly doubled the amount of October-March. This seasonality in WAIS might be related to storms forming in the Pacific Ocean and anticyclonic events in the ABS that occur more often during winter (Emanuelsson et al., 2018; Sinclair & Dacre, 2019). Precipitation rates in the Weddell Sector (Figure 3.4-E) were $\approx$1 mm day^{-1} during MAM and SON, whereas DJF and JJA were over 30% drier. According to Sinclair & Dacre (2019), there is no storm contribution to meridional moisture flux during summer and winter in the Weddell Sea.

Regarding the reanalyses performance, 20Cv3 and CFSR had larger PPT while the ECMWF's products (Era20C and EraInt) were drier. For instance, (1) 20Cv3 was +0.5 mm day^{-1} more humid than MRM7 during all months in EAIS (Figure 3.4-B); or (2) in the Weddell Sector, PPT for EraInt was up to 40% less than for MRM7 (Figure 3.4-E). These results agree with Appendix-A.

In the Austral region (Figure 3.5-A), the PPT in each month were equal – the curves overlap – for MRM7 and the multi-model mean (MMM23). It suggests that the simulations correctly represent seasonal variations of rainfall if considering the averaged 60°-90° S area. From a regional perspective, though, the models overestimated PPT in comparison with MRM7.

The weak seasonal cycle of EAIS is characterized by minimum/maximum PPT during SON/DJF (Roussel et al., 2020). Such a pattern appeared in the models, but MMM23 doubled the values of MRM7 during summer (Figure 3.5-B). In the W-WAIS/Ross Sector (Figure 3.5-C), the amount of PPT for MMM23 exceeded MRM7 in all months, especially in April and August (+0.3 mm day^{-1}). From June to January, simulated (MMM23) PPT were 10% higher than for MRM7 in E-WAIS/Amundsen Sector (Figure 3.5-D). Except for DJF, MMM23 was +0.2 mm day^{-1} wetter than MRM7 in the Weddell Sector (Figure

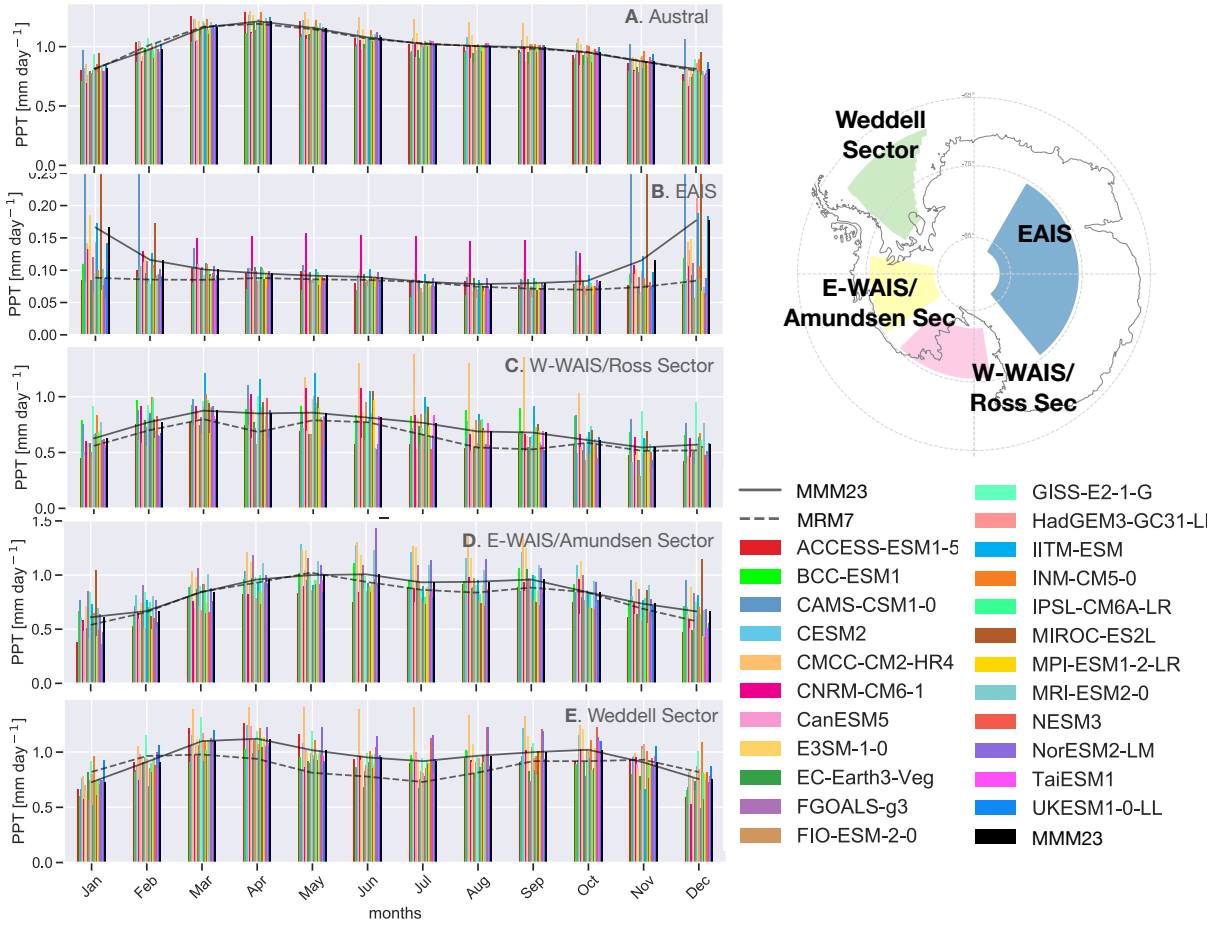

Figure 3.5: Climatological 1900-2014 seasonal cycle of PPT, in mm day^{-1}. Panels A-E represent Antarctic regions, as indicated by the map on the label. The bars correspond to individual models, and the solid line refers to MMM23. To allow comparison with the reanalyses, MRM7 is overlapped as the dashed line. Note the different y-axis scales on each panel.

3.5-E).

Former studies concluded that CMIP models are wet-biased (Krinner et al., 2007; Palerme et al., 2017b). As pointed by Roussel et al. (2020) and showed in Figure 3.5, individual CMIP6 models, plus the multi-model mean, are able to reproduce the PPT seasonal variability, albeit with higher values. Each region presented highly biased simulations, like models #C, #G, and #Q in EAIS, or model #F in W-WAIS/Ross and Weddell sectors (labels as in Table 2.2). The EAIS region during summer was the most biased (Figure 3.5-B).

3.2.3 Temporal variability and trends

Figure 3.6 displays how regional precipitation developed between the years 1900 and 2014 in each reanalysis. Agreeing with sections 3.2.1 and 3.2.2, 20Cv3 and CFSR reanalyses had more rainfall in all regions, whereas the ECMWF's products (Era20C and EraInt) and NCEP2 were drier. Tang et al. (2018) investigated PPT in the averaged area of 60°-90° S during 1979-2005 using reanalyses, and found that CFSR/EraInt had highest/lowest values as well. Regardless, the reanalyses' spread were generally confined within the 95% confidence interval (CI = $MRM7\ mean \pm 1.96STD$) – aside from 20Cv3 in EAIS (Figure 3.6-B) and E-WAIS/Amundsen Sector (Figure 3.6-D) after 1980. Note that MRM7 presents discontinuities in 1979-1980 (more evident in EAIS), which occurs due to the ensemble size expanding from the two 20th-century products to seven reanalyses total.

Throughout 1900-2014, the average PPT poleward of 60° S was 0.9 mm day^{-1} (Figure 3.6-A). Previous studies stated that the Austral region has experienced enhanced PPT at least since the last 200 years (Thomas et al., 2017; Tang et al., 2018; Medley & Thomas, 2019; IPCC, 2021). Not only PPT has increased, but its upward trend accelerated after 1979; trends estimated for MRM7 were 8.2e-3 and 1.3e-2 mm day^{-1} decade^{-1} during 1900-1979 and 1980-2014, respectively – a growth of nearly 60% (Figure 3.6-A). In both periods, the statistical significance of the trends exceeded the 99% level. To allow comparison, in Medley & Thomas (2019), snow accumulation trends increased 150% from 1901-2000 (0.4 Gt year^{-2}) to 1957-2000 (1 Gt year^{-2}) over AIS. Bromwich et al. (2011) found higher accumulation trends in 1989-2009 compared to the 1979-2009 south of 60° S using five reanalysis products. Figure 3.7-C details the Austral trends for each reanalysis; During "B1980" (1900-1979), the two products available showed significant (p-value $<$ 0.01) positive trends. From 1980 onwards, Era20C, JRA55, MERRA2, and NCEP2 had positive and significant trends, opposite to negative and with p-value $>$ 0.05 values for 20Cv3, CFSR, and EraInt.

In the desert EAIS, the average precipitation rate was 0.09 mm day^{-1} (Figure 3.6-B),

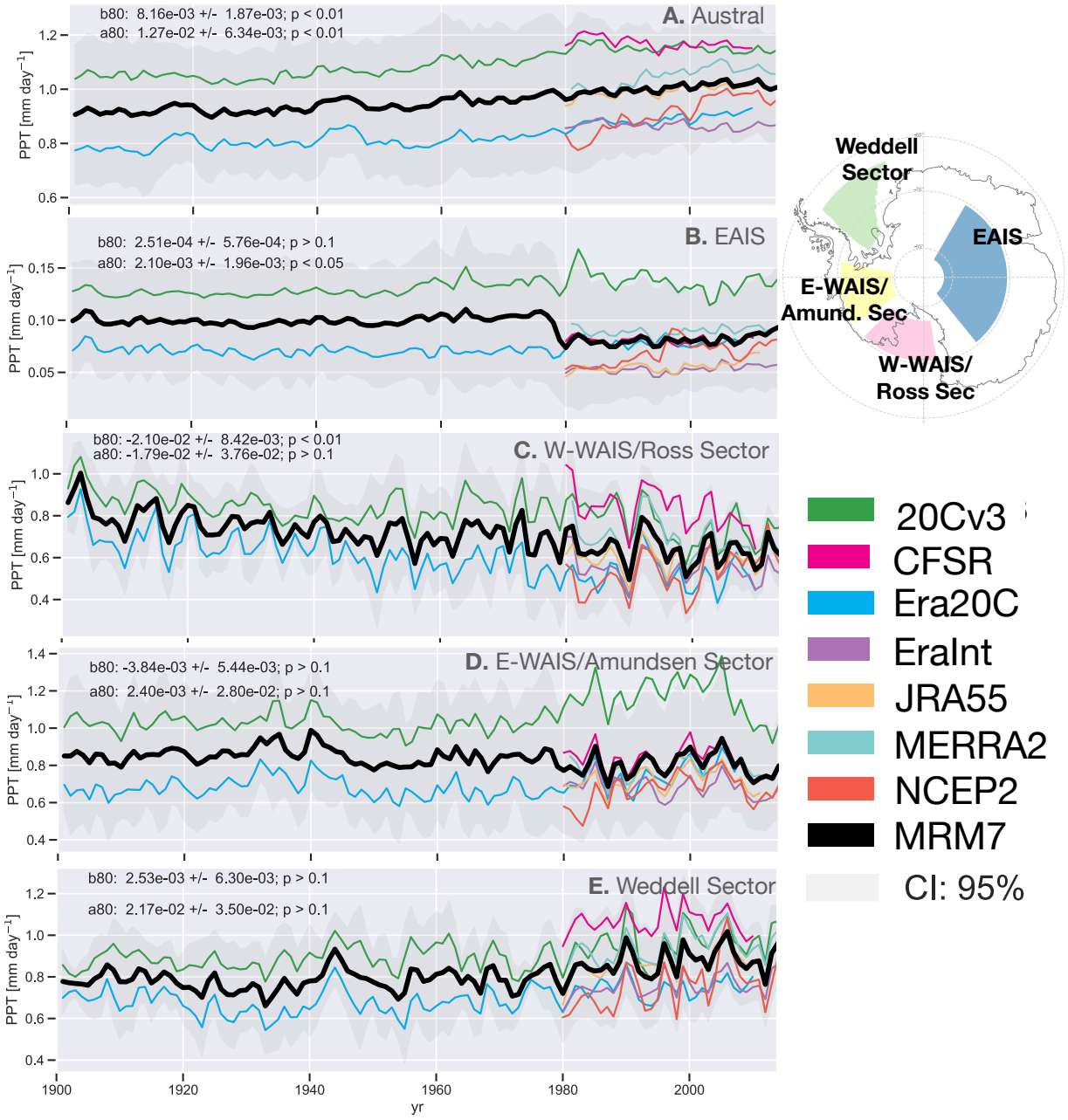

Figure 3.6: PPT time series from 1900 to 2014. Panels A-E represent Antarctic regions, as indicated by the map on the label. The colored lines correspond to individual reanalyses, and the thick black line refers to MRM7. Gray shading shows the MRM7 95% confidence interval (CI total width = $MRM7\ mean \pm 1.96 STD$). The regional MRM7 trends during "B1980" (1900-1979) and "A1980" (1980-2014) periods and their statistical significance (p-value) are exhibited as text on each panel.

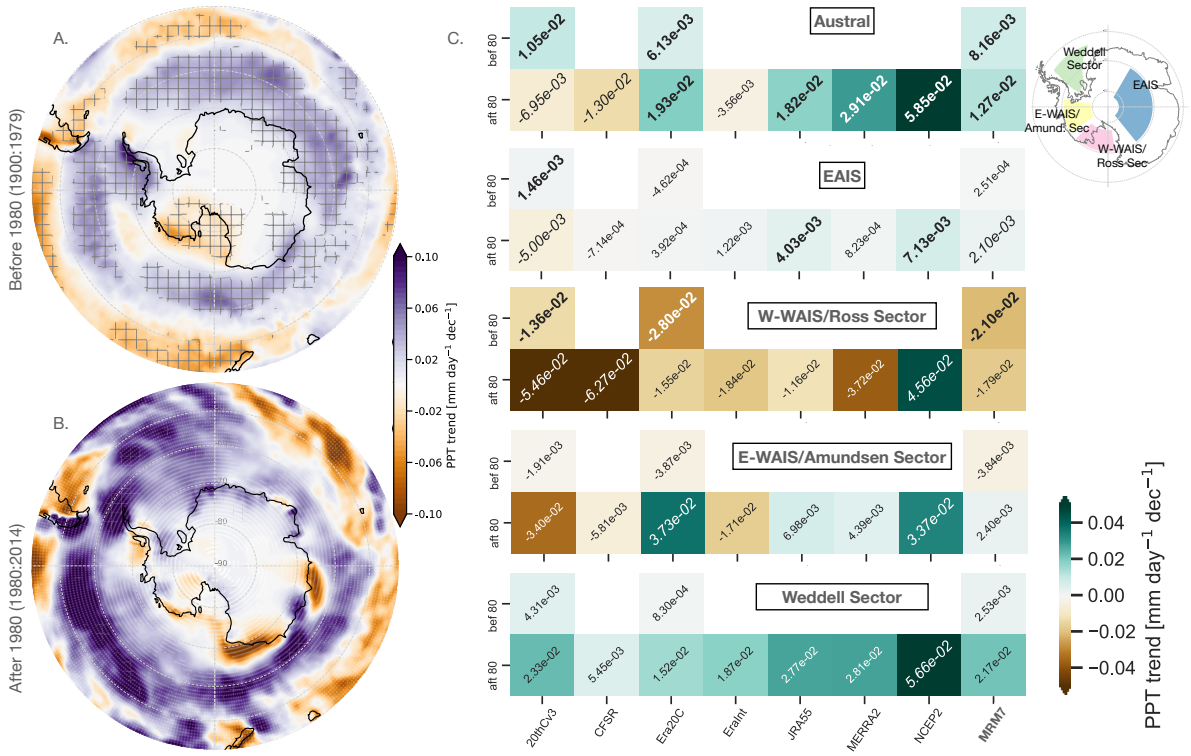

Figure 3.7: PPT trends before and after 1980. The left column displays the spatial pattern of PPT trend for MRM7 during (A) "B1980" (1900-1979) and (B) "A1980" (1980-2014). Purple/orange mean regions with more/less precipitation. Cross-hatched and stippling refer, respectively, to the statistical significance (p-value < 0.05) and reanalyses agreement (at least 6 out of 7 reanalyses) with respect to the trend. On panel C: regional PPT trends during "B1980" (upper row) and "A1980" (lower row), in mm day^{-1} decade^{-1}, for individual reanalysis and MRM7. Reanalyses with data starting in 1979 appear as blank spaces in the top ("before 1980") row. Each panel from top to bottom represents an Antarctic region, as indicated by the map on the label. Green/brown stands for positive/negative trend values. The text format designates the statistical significance of the trend: **bold**, *italic*, and small font size indicates p-values < 0.01, < 0.05, and > 0.05, respectively.

revealing no interannual variability nor significant (p-value > 0.1) changes before 1980. Even during the later period, in which the MRM7 trend was significant at the 95% level, it had a negligible value compared to other regions (2.1e-3 mm day^{-1} decade^{-1}); The trend values in EAIS were minimal for all reanalysis (Figure 3.7-C). Studies that use contemporary data (from 1979 onwards), as Bromwich et al. (2011) or Tang et al. (2018),

confirm unchanged PPT over the Antarctic plateau; so do studies that extend back to the past through climate reconstruction as Thomas et al. (2017) or Medley & Thomas (2019). In fact, Thomas et al. (2017) estimated accumulation trend of value zero within 1911-2010 in EAIS.

The dry W-WAIS/Ross Sector presented an average PPT of 0.6 mm day^{-1} throughout 1900-2014 (Figure 3.6-C). Turner et al. (2019) notes that the topography surrounding this area favors off-continent winds that block moisture penetration, thus resulting in less rainfall. Prior to 1980 (1900-1979), PPT decreased at a rate of -2.1e-2 mm day^{-1} decade^{-1} (p-value < 0.01); after 1980 (1980-2014), the trend was still negative with a value -1.8e-2 mm day^{-1} decade^{-1}, though the statistical significance was up to the 90% level (Figure 3.6-C). All reanalyses but NCEP2 agreed on the sign of the trend (Figure 3.7-C). Medley & Thomas (2019) ratify this rainfall decrease in W-WAIS/Ross Sector during 1901-2000, notably more intense between 1957-2000. Turner et al. (2019) and Wille et al. (2021) directly link the PPT drop in western-WAIS and the Ross Sea, with the penetration of atmospheric rivers becoming scarcer since 1979. Such reduction of rainfall from 1900 into the 21st century seems to be deeply related to changes in atmospheric circulation (Irving & Simmonds, 2015; Turner et al., 2019; Wille et al., 2021; Medley & Thomas, 2019); The mechanisms that drive such changes are explored in section 3.5.3.

E-WAIS/Amundsen and Weddell sectors (Figures 3.6 D and E) were the regions with more rainfall in this study, with PPT averages of $\approx$0.8 mm day^{-1} within 1900-2014.

Looking at individual reanalysis products over the eastern-WAIS and the Amundsen Sea areas (Figure 3.7-C), the only estimates that exceeded the 95% level of significance were positive trends for Era20C and NCEP2 in the "A1980" period (1980-2014). The trends were not significantly different from zero (p-value > 0.1) for the multi-reanalysis mean (Figure 3.6-D), which conflicts with the literature that discusses substantial PPT enhance in this area (Lenaerts et al., 2013; Goodwin et al., 2016; Thomas et al., 2015; Thomas et al., 2017). Such a weak trend in the averaged E-WAIS/Amundsen Sector area could possibly have occurred due to the regional boundary we defined in Section 2.2.1, separating western- and eastern-WAIS in 130° W. But, looking at the MRM7 PPT trends'

spatial pattern, the dipole of rainfall changes across WAIS reveals — more/less PPT in eastern/western WAIS (Figure 3.7 A and B). Medley & Thomas (2019) similarly showed a remarkable snow accumulation trend dipole between eastern- and western-WAIS during 1901-2000.

Regarding the Weddell Sea region, individual reanalysis plus their ensemble mean (MRM7) showed PPT gains during both periods, with the trends' statistical significance of up to 95% (Figures 3.6-E and 3.7-C). Information about PPT changes on the oceanic area of the Weddell Sea is limited: Thomas et al. (2017) calculated a +0.4 Gt year^{-2} snow accumulation trend through 1911-2010, but at the Weddell shore rather than over the sea; Nicolas & Bromwich (2011b) plotted PPT trend maps for the Austral region during 1989-2009 in different reanalyses where, in the Weddell Sea, they conflicted in both sign and values. Up to this date, we could not find studies that precisely quantify how much PPT changed over the Weddell Sector.

Much is argued regarding weak or non-statistically significant precipitation trends over the Antarctic Ice Sheet (Monaghan et al., 2006, Bromwich et al., 2011, Nicolas & Bromwich, 2011b, Lenaerts et al., 2013). It is critical noticing, though, that regional PPT changes mask a continental-wide signal – gains in one region offset losses in another, and their effects cancel out (Fyke et al., 2017). The multi-reanalysis mean (MRM7) showed that Antarctica underwent an overall PPT increase during both "B1980" and "A1980" periods (Figure 3.7). Yet, contrasting results appear when talking a detailed regional perspective.

For instance, W-WAIS/Ross Sector experienced a precipitation drop in both periods (Figure 3.7-A), while western/eastern AP exhibited positive/negative PPT trends – which may be related to the circumpolar trough strengthening and intensification of the Foehn effect (Bozkurt et al., 2021). As discussed by Irving & Simmonds (2015) and Fyke et al. (2017), the alternating PPT trend sign on the Antarctic coastline during "A1980" hints a ZW3 pattern (Figure 3.7-B): enhanced PPT in Dronning Maud Land (5° W-30° E), Wilkes Coast, and eastern-WAIS, oppose to negative trend values in western-WAIS/Ross Sea, Weddell seashore, and at the Davis Sea (90°-105° E; see locations in Figure 2.1).

The spatial pattern of rainfall drop occurring in the 40°-50° S oceanic area – contrary to enhanced PPT in the SO – maintained all along 1900-2014, but the PPT trends intensified after 1980 (Figures 3.7 A and B).

Time series of precipitation rates within 1900-2014 for the CMIP6 simulation results are displayed in Figure 3.8. Due to the larger ensemble size, which masks the interannual variability effect, the MMM23 regional curves are flattened. Except for #C and #Q (labels as in Table 2.2) being positively biased, the other models – plus MRM7 – lay within the 95% confidence interval around MMM23 (CI = *MMM23 mean* ± *1.96STD*). PPT values for MMM23 matched MRM7 in western and eastern-WAIS regions in both periods, and in EAIS during "B1980"; MMM23 exceeded MRM7 in Austral (+5%) and Weddell Sector (+19%) over 1900-2014, and in EAIS (+33%) since 1980. These results reinforce the wet bias of CMIP6 models (Roussel et al., 2020).

Concerning the PPT trends, MMM23 in the averaged area of 60°-90°S was consistent with MRM7 and with former studies (Medley & Thomas, 2019; IPCC, 2021). It captured a general PPT rise throughout 1900-2014; More, comparing PPT trends in the two periods, the latter was sevenfold larger (increased from 2.1e-3 to 1.5e-2 mm day^{-1} decade^{-1}, with p-value < 0.01 in both). MMM23 fairly represented PPT changes in EAIS as well (Figure 3.9-C): trends on the Antarctic plateau were virtually zero, similar to the multi-reanalysis mean (Figure 3.6) and previous studies (e.g., Tang et al., 2018).

Unlike the Austral and EAIS regions, the trends estimated for MMM23 deviate from MRM7 in the W-WAIS/Ross sector (Figure 3.9-C). The reanalyses showed a robust (p-value < 0.01) drop in PPT but the trends for the multi-model mean were minor, positive, and not statistically significant (p-value > 0.05) during the two periods. Examining individual simulations revealed no model agreement in this region (Appendix-B): eleven out of 23 models agree with MRM7, capturing the PPT decrease for both "B1980" and "A1980" periods. The CMIP6 models seem to have difficulty representing PPT changes across western-WAIS and the Ross Sea, and the MMM23 was unable to reproduce the observed rainfall variations throughout 1900-2014 described by Medley & Thomas, 2019 and Wille et al., 2021.

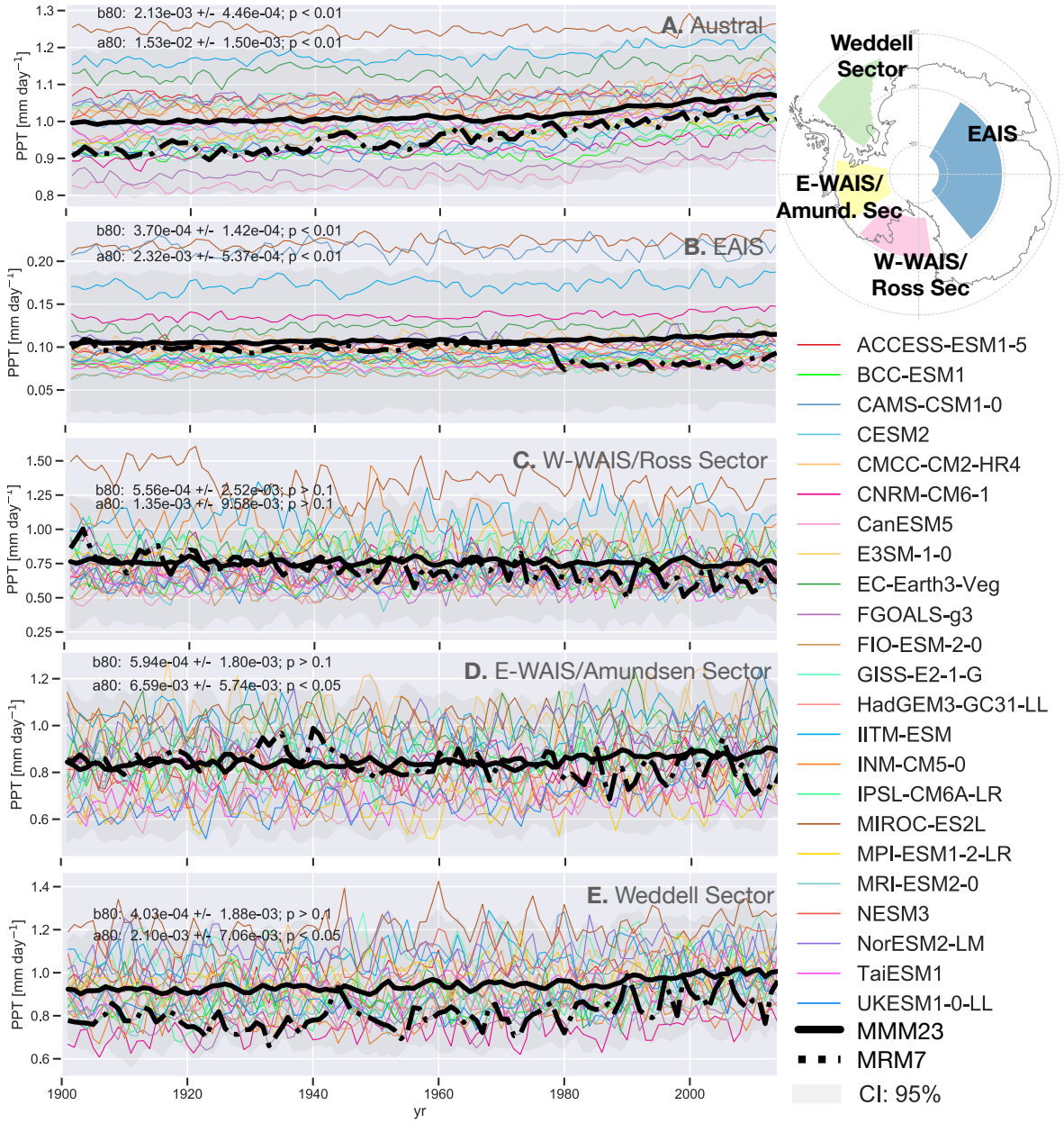

Figure 3.8: PPT time series from 1900 to 2014. Panels A-E represent Antarctic regions, as indicated by the map on the label. The colored lines correspond to individual models, the thick solid black line to MMM23, and the thick dashed black line to MRM7. Gray shading shows the MMM23 95% confidence interval (CI total width = *MMM23 mean* $\pm$ $1.96STD$). The regional MMM23 trends during "B1980" (1900-1979) and "A1980" (1980-2014) periods and their statistical significance (p-value) are exhibited as text on each panel.

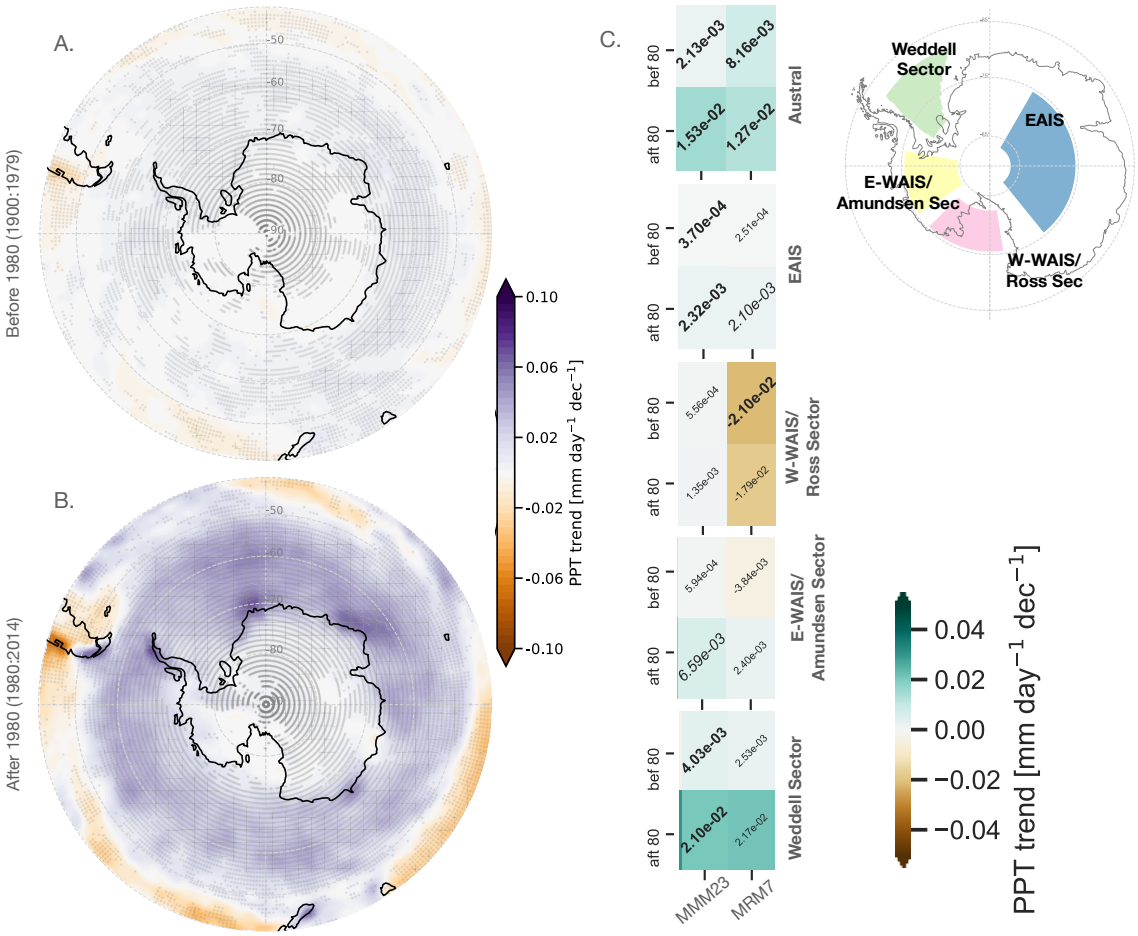

Figure 3.9: PPT trends before and after 1980. The left column displays the spatial pattern of PPT trend for MMM23 during (A) "B1980" (1900-1979) and (B) "A1980" (1980-2014). Purple/orange mean regions with more/less precipitation. Cross-hatched and stippling refer, respectively, to the statistical significance (p-value < 0.05) and model agreement (at least 15 out of 23 models) with respect to the trend. On panel C: regional PPT trends during "B1980" (upper row) and "A1980" (lower row), in mm day^{-1} decade^{-1}, for MMM23 and MRM7 (to allow comparison; same values as in Figure 3.7). Each panel from top to bottom represents an Antarctic region, as indicated by the map on the label. Green/brown stands for positive/negative trend values. The text format designates the statistical significance of the trend: **bold**, *italic*, and small font size indicates p-values $<$ 0.01, $<$ 0.05, and $>$ 0.05, respectively.

No PPT changes occurred in E-WAIS/Amundsen Sector for MMM23 (Figures 3.8-D), agreeing with our findings for the multi-reanalysis mean in Figure 3.6-D. That implies in neither our datasets capturing the enhanced PPT in eastern-WAIS/southern AP found

by Medley & Thomas (2019) or Thomas et al. (2017). The CMIP6 models showed small positive PPT trends in the Weddell Sector, with an acceleration since 1980, like shown by MRM7 (Figures 3.6 and 3.8 E).

The maps in Figure 3.9 reveal a boost of the PPT trends after 1980. In the two periods – like for the reanalyses in Figure 3.7 – negative trends happened north of 50° S, opposing to enhanced Austral rainfall. Inland Antarctica, the in trends imply that the CMIP6 models could not reproduce regional changes in PPT throughout 1900-2014.

3.3 Atmospheric dynamics

By distinguishing AMIP from CMIP, it becomes possible to understand the role that subsurface ocean dynamics play in the high southern latitudes PPT. In this sense, Figure 3.10 displays the comparison between three sets of data: coupled models (MMM23), atmospheric models (AMIP), and reanalysis (MRM7), which are the reference value in this study.

The annual cycle of PPT for AMIP in Figure 3.10-A mimics the curve for MMM23, although exhibiting slightly lower values. Studies have pointed that SST being positively biased in the coupled models results in higher PPT (Palerme et al., 2017b; Roussel et al., 2020). For this reason, in Figure 3.10-A, it is observed that the curves of PPT for AMIP are closer to the reference value (MRM7) than the coupled models.

Figure 3.10-B shows the spatial pattern of the difference between AMIP and MMM23 (Δ = AMIP - MMM23). In most of the area southern than 40° S, the coupled models presented higher PPT than the atmospheric-only ones ($\Delta < 0$). Particularly, the difference was less than zero in the entire Austral region. The disparity between the experiments may be negligible in some areas (null inland Antarctica) or substantial in others; For instance, the larger Δ values ($\approx$ -0.3) were found over the SO between 0°-45° E, where the average PPT was approximately 3 mm day^{-1} according to Figures 3.2 and 3.3. That is to say that, in this region, PPT in MMM23 is up to 10% more than in AMIP.

These findings suggest that the ocean-atmosphere feedbacks – incorporated in the

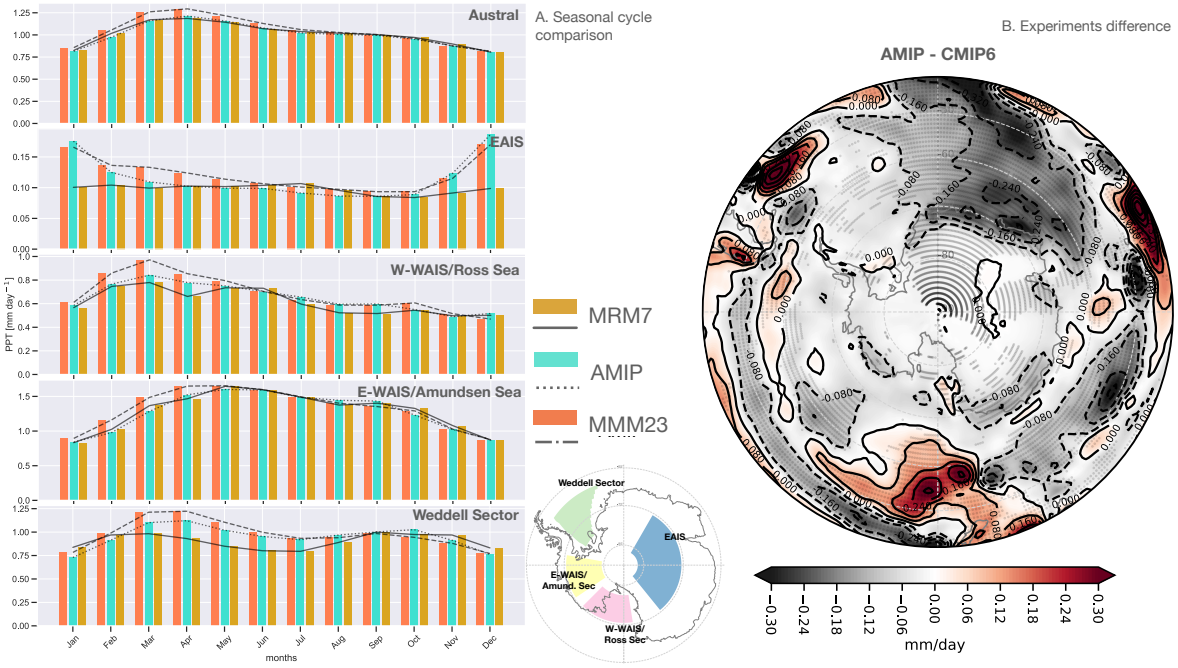

Figure 3.10: On panel A, the climatological 1979-2014 seasonal cycle of PPT, in mm day^{-1}. Each panel from top to bottom represents an Antarctic region, as indicated by the map on the label. Gold/Turquoise/Orange bars and solid/dotted/dashed lines relate to MRM7/AMIP/MMM23. Panel B shows the difference between the experiments AMIP (atmospheric-only models) and MMM23 (coupled models) (Δ = AMIP - MMM23). Red/Black shading indicates more PPT in the AMIP/MMM23 experiment. Stippling indicates model agreement on the sign of the difference at the 95% significance level (15 out of 23 models agree).

coupled models configuration – act to enhance the PPT in Antarctica.

3.4 Sea surface temperature and its influence on precipitation

As it is understood that the ocean (moisture source) and the ocean-atmosphere feedback (water cycle) are central explanations for precipitation in Antarctica, we now investigate how the SST changed from 1900 to 2014.

3.4.1 SST trends

The multi-reanalysis mean in Figure 3.11-A show that the SO underwent a significant (p-value < 0.05) warming during 1900-1979, spanning 0 to 0.3 °C decade^{-1}. The study of Gille (2008) confirms progressive increases of SST in the SO between 1930-1990. In contrary to most areas south of 40° S, the Pacific Ocean and the Amundsen-Bellingshausen Sea (ABS) regions exhibited negative trends (-0.25-0 °C decade^{-1}, with p-value < 0.05) in the "B1980" epoch (Figure 3.11-A). Less than 6 out of 7 reanalyses agreed on the sign of the trend, probably owing to SST measures at different depths for each product ("skin temperature" for 20Cv3, CFSR and NCEP2; "brightness temperature" for JRA55; and "sea surface temperature" for Era20C, EraInt, and MERRA2). Regardless, the spatial pattern of SST trends for MRM7 was similar to that of the observations (Appendix-C), indicating that the multi-reanalysis mean coincides with reality.

SST trends from 1900 to 1979 for the multi-model mean were virtually zero in the whole region south of 40° S (Figure 3.11-B). Over some areas of the Pacific Ocean and the ABS, where the reanalysis showed cooling, MMM23 exhibited no model agreement nor trends significantly different from zero (p-value > 0.05).

From 1980 onwards (1980-2014), an inversion occurred on the trend sign, with negative SST trends appearing over the ocean south of 50° S (Figure 3.11-C). The spatial pattern of SST trends in MRM7 matches observations during "A1980" (Appendix-C). Numerous studies endorse the SO's cooling since 1979 and propose two principal mechanisms responsible for it: (1) the westerlies' strengthening that followed ozone depletion and GHG concentration increases since 1970, which intensifies the Ekman drift, pushing cold coastal waters and sea ice from Antarctica further north; and (2) the SO's freshening that increases surface stratification and impedes convective mixing with warmer subsurface waters (Hall & Visbeck, 2002; Purich et al., 2016; Spence et al., 2014; Kostov et al., 2018; Doddridge et al., 2019; Auger et al., 2021).

The SST trends in CMIP6 simulations during 1980-2014 do not agree with the Reanalysis at all (Figure 3.11-D). There is a clear warm bias south of 50° S, which have already

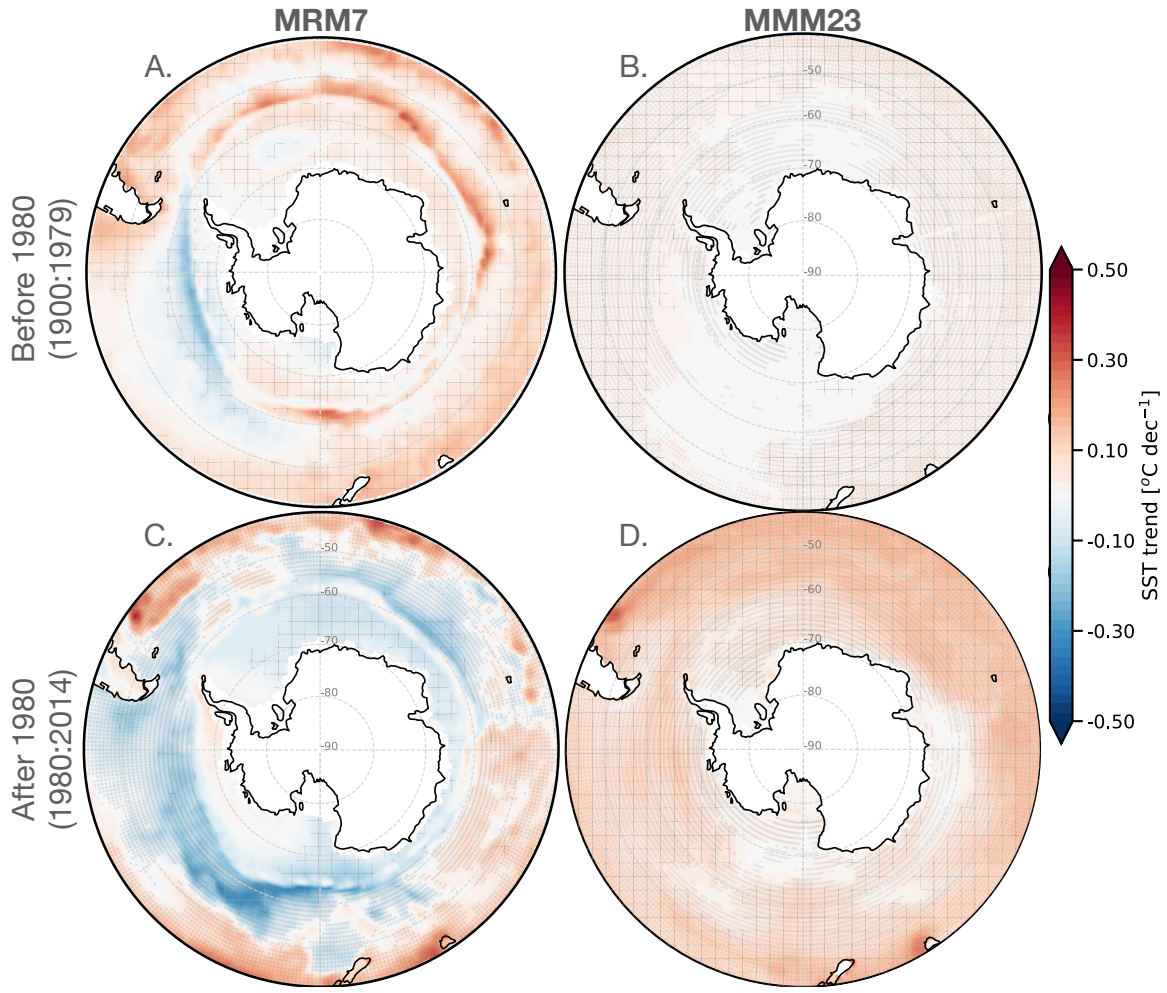

Figure 3.11: Sea surface temperature trends, in °C decade^{-1}. Left panels refer to MRM7 (A and C) and right panels to MMM23 (B and D). The top row (A and B) attributes to SST trends "B1980" (1900-1979), and the lower row (C and D), to trends "A1980" (1980-2014). Red/blue shading: warmer/cooler regions. Cross-hatching/stippling indicates where the trend/dataset's agreement is significant at a 95% significance level.

been discussed in many studies (Hyder et al., 2018; Zhang et al., 2019; Beadling et al., 2020; Wang et al., 2021a). Virtually all grid points show that more than 15 models (out of 23) agree with the trend signal, implying a systematic problem with coupled models in reproducing the SST time variation rather than defects in individual products. The hypotheses explaining such problems are cloud-related shortwave biases (Hyder et al., 2018; Wang et al., 2021a) or underestimated changes in westerly winds (Purich et al., 2016; Beadling et al., 2020).

Although the CMIP6 simulations, particularly their ensemble mean, have been shown to reproduce the SST field (Figure 3.1-B), they failed in simulating its temporal evolution. Given that the results produced by the models are controversial, the next analyses were carried using only Reanalysis products.

3.4.2 Correlation between the SO's SST and regional PPT

Beyond the trends, we addressed the multi-reanalysis mean (MRM7) correlations between the SST field south of 40° S and the PPT time series for the regions defined in Section 2.2.1 (same time series as in Figure 3.6).

The EAIS region showed weak-to-moderate negative correlations ($-0.5 < r < 0$) and no particular area over the ocean that could be the origin of moisture for the plateau (Figure 3.12-A); Delaygue et al. (2000) stated that "the moisture supplied to a given area of Antarctica originates primarily from the adjacent ocean basin" thus, we expected a direct link between the Indian Ocean and the EAIS. The correlations reinforce the importance of atmospheric circulation delivering moisture through air masses in EAIS (Turner et al., 2019) rather than a direct link with SST.

The ASL highly influences the climate in WAIS, AP, and the Weddell Sea regions (Thomas et al., 2015; Fyke et al., 2017; Turner et al., 2019; Wille et al., 2021). Consequently, these three regions manifested a peculiar relationship between regional PPT and SST over the ABS (Figures 3.12 B, C, and D). The spatial pattern of correlations was similar in both WAIS subregions: PPT was anticorrelated with SST ($r < 0$) in most of the ocean southern than 40° S, and positively liked over the ABS ($r > 0$; Figures 3.12 B and C). At least 6 out of the seven reanalyses agreed on the correlation sign over those regions.

In the Weddell Sector, the correlation mimics what was observed for the WAIS subregions but with a reversed sign (Figure 3.12-D); Positive coefficients ($0 < r < 0.5$) appeared over the ocean and negative ($-0.4 < r < -0.2$) in the ABS. The study of Thomas et al. (2017) suggested a possible connection between PPT in the Weddell Sea region and the sea surface conditions over the Bellingshausen Sea.

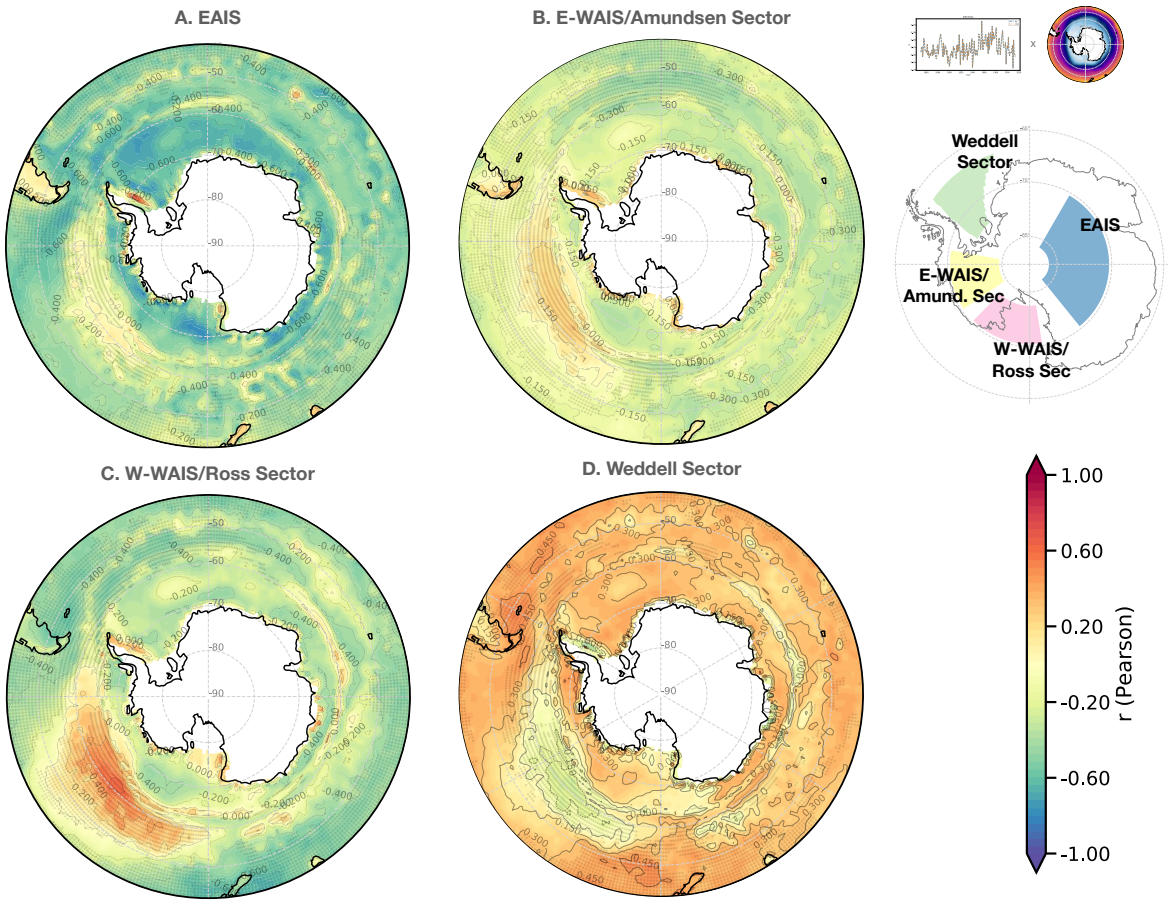

Figure 3.12: Pearson correlation (r) between the SST field and regional PPT time series for the multi-reanalysis mean (MRM7). Panels A-D represent Antarctic regions, as indicated by the map on the label. Stippling shows where at least 6 out of 7 reanalyses agree on the correlation sign.

The inverted correlation signs between WAIS subregions and the Weddell Sea hints at the ASL seasonal and interannual movement: when it migrates south-westwards (north-eastwards), its eastern flank places over WAIS (AP), allowing more northerly humid winds penetrating such region (Thomas et al., 2015; Bracegirdle et al., 2020).

3.4.3 Is it possible to establish a causal relationship of changes between the SO's SST and regional PPT?

To try and find if variations in the Southern Ocean sea surface temperature drove precipitation changes in Antarctica, we explored their linear fit (Figure 3.13).

The variables – PPT trend and SST trend – exhibited a good fit before 1980 (1900-1979), with R-squared within 80%-100%; This suggests a strong causal relationship implying that PPT changes happened due to SST trends. However, one must be cautious on the statistical significance of this result, as only two reanalyses were available during this period, and the trends for both variables were nearly zero. In any case, it showed an inverse relationship between PPT trends and SST trends in all regions, indicating that the ocean warming observed in the "B1980" period (Figure 3.11-A) could be associated to rainfall reduction.

The W-WAIS/Ross Sector – which indeed became drier over this period (Thomas et al., 2017) – had the largest sensitivity of -0.27 mm day^{-1} °C (Figure 3.13-I). Our findings for MRM7 in EAIS and E-WAIS/Amundsen Sector showed no PPT changes before 1980 (Figure 3.6), which may explain the strong link with the virtually-zero SST trends. The suggestion that ocean warming would reduce PPT in the Weddell Sector (-0.06 mm day^{-1} °C) does not agree with our estimates (e.g., Figure 3.7); Thus, another mechanism must be responsible for such rainfall changes in this region.

From 1980 to 2014, the R-squared was up to 5% in all regions. Such weak linear fit implies that variations in SO's SST contributed to only a small fraction of the PPT changes in Antarctica – that were, therefore, determined by other mechanisms. Anticorrelations between SST trends and PPT trends suggest that the SO cooling since 1980 (Figure 3.11-C) caused more rainfall in Austral, Weddell Sector, and W-WAIS/Ross Sector (Figures 3.13 B, D, and J). This relationship agrees with Figure 3.7 in Austral and Weddell Sector but challenges the PPT drop in W-WAIS/Ross Sector.

Kittel et al. (2018) ran a sensibility test in order to evaluate the percentage of rainfall over the Antarctic Ice Sheet that would change per degree of SO warming; They found

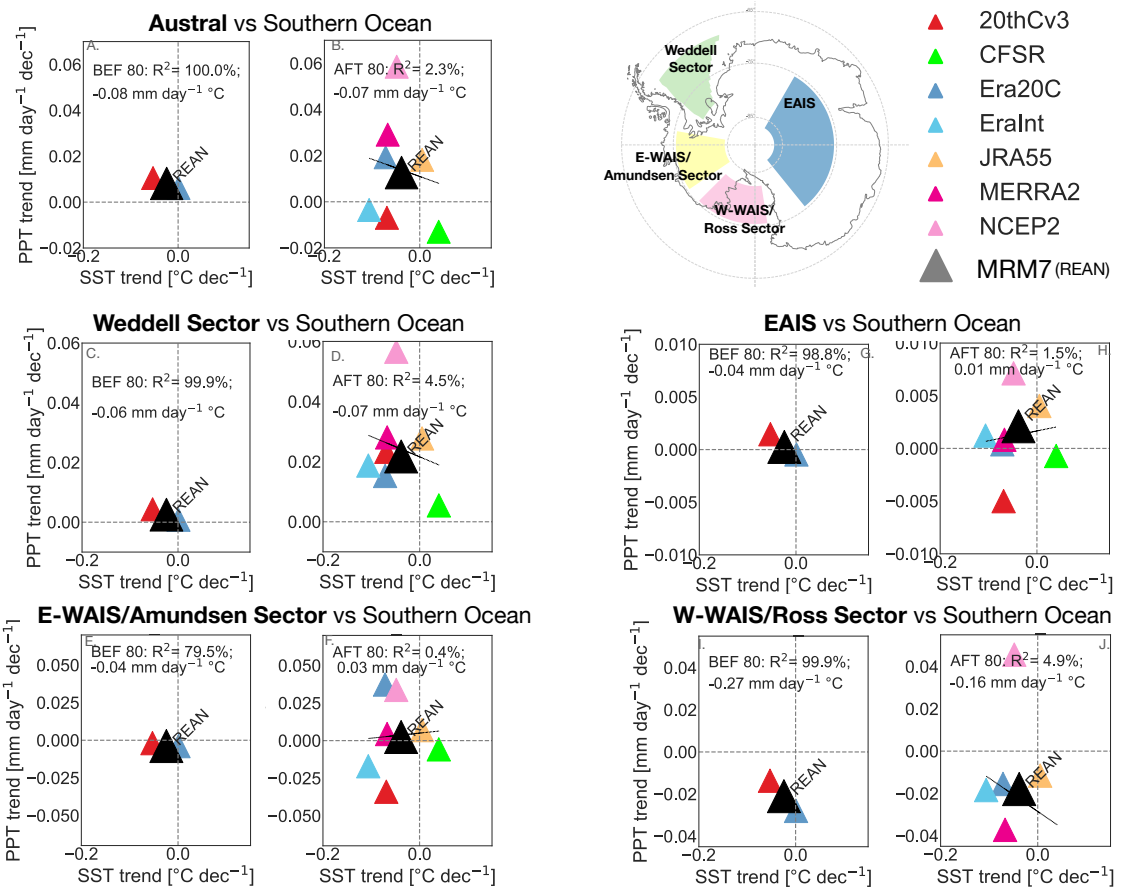

Figure 3.13: Linear least-squares regression between SST trends in the SO (south of 60° S) and regional PPT trends for individual reanalysis and MRM7. Each panel represents an Antarctic region, as indicated by the map on the label. Panels A, C, E, G, and I refer to the period "B1980" (1900-1979) and B, D, F, H, and J, to "A1980" (1980-2014). Note that only two reanalyses are available (20Cv3 and Era20C) in the later period. The text shows statistics from the linear fit: the R-squared and the sensitivity, in mm day^{-1} decade^{-1}.

an intrinsic relationship between increased SST prompting higher evaporation and more moisture content in the air, which led to greater PPT in the Antarctic coastline. Over the plateau, conversely, SO warming would lead to drier conditions. The opposite occurs when the Southern Ocean cools, with negative (positive) PPT anomalies in coastal (plateau) areas. Our results (Figures 3.7 and 3.13) revealed mainly longitudinal contrasts of PPT changes that reflect atmospheric circulation patterns (e.g., the ZW3) rather than altitude-related changes.

Schneider et al. (2020) analyzed the response of PPT in the face of two mechanisms: (1) surface warming and (2) changes in the circumpolar trough (strengthening and migration southward); Their results show that the thermodynamical forcing (SST changes) was more expressive seasonally, while the dynamical forcing (trough changes) predominates in the long term. The study of Schneider et al. (2020) concluded that changes in the westerly winds – particularly the southward migration – are the primary mechanism for Antarctic rainfall increases under an ozone depletion scenario.

3.5 Changes in the atmospheric circulation

We have shown that despite the importance of ocean-atmosphere interactions (section 3.3), variations in the Southern Ocean's SST were not the primary mechanism driving precipitation changes during 1900-2014 in Antarctica (section 3.4.3). We now explore the atmospheric circulation conditions during this epoch and its connection with PPT.

3.5.1 500 hPa meridional wind and its link to PPT

As presented in former studies, like in Nicolas & Bromwich (2011a), Thomas et al. (2017), and Donat-Magnin et al. (2020), northerly flow brings moisture from the ocean into Antarctica. For this reason, in Figure 3.14, it is observed anticorrelations between V-wnd and regional PPT during 1900-2014. In other words, negative V-wnd velocity (northerly winds) enhances PPT. In EAIS, the correlation between meridional wind speed and PPT rates was weak (from -0.3 to 0, in Figure 3.14-A), and showed a C-shaped area with a negative r over the plateau, also noticed by Rodehacke et al. (2020).

According to Donat-Magnin et al. (2020), the precipitation in E-WAIS/Amundsen Sector increases when the ASL migrates south-westwards, placing a northerly flow over this region. Figure 3.14-B displays anticorrelations ($r \approx -0.3$) around 150° W, alternating with positive correlations in the Weddell Sea and Victoria Land (120°-180° E, location in Figure 2.1) regions. These alternating correlation signs suggest a cyclonic circulation (the ASL) over the Amundsen Sea and an anticyclone between the Bellingshausen and

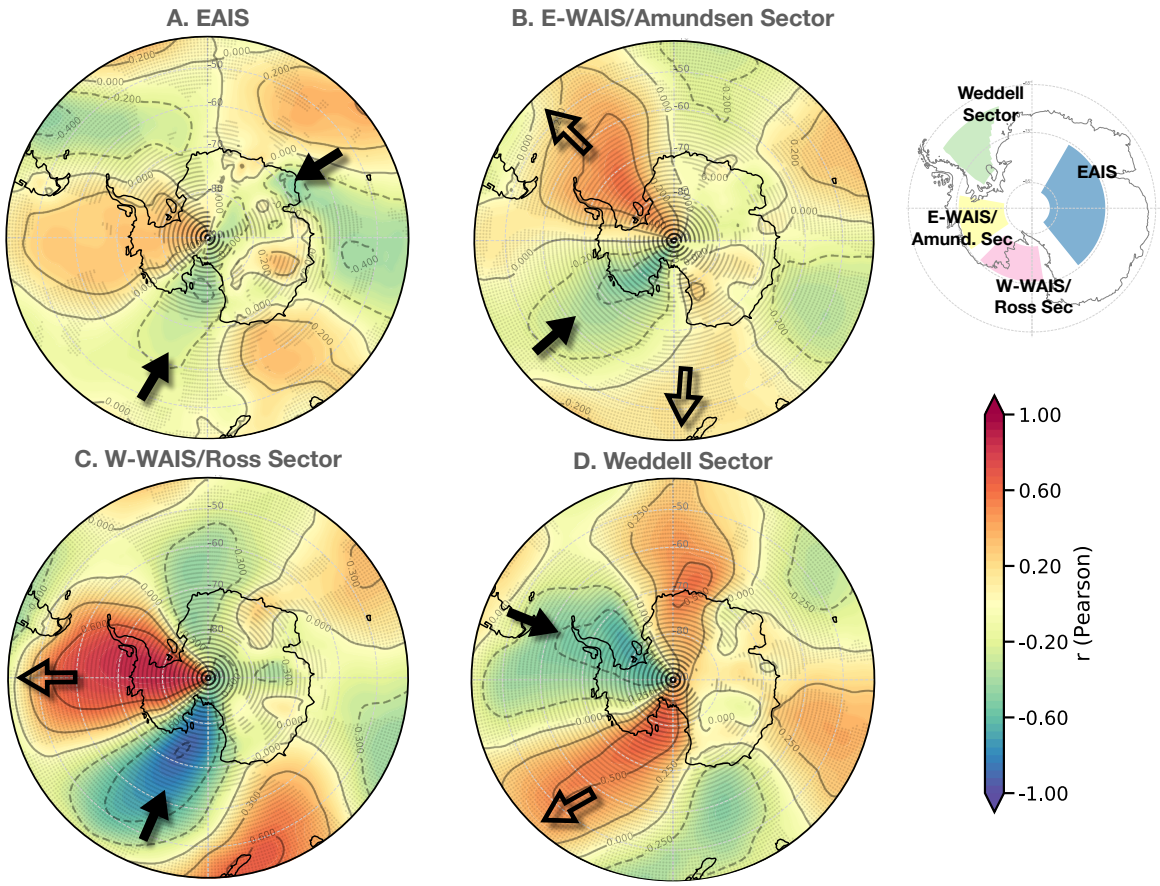

Figure 3.14: Pearson correlation (r) between the V-wnd field and regional PPT time series for MRM7. Panels A-D represent Antarctic regions, as indicated by the map on the label. Stippling shows where at least 6 out of 7 reanalyses agree on the correlation sign.

Weddell seas. Both advect moist air masses from the ocean to E-WAIS/Amundsen Sector.

Compared to other regions, the strongest correlations appeared in W-WAIS/Ross Sector (Figure 3.14-C). It exhibited a southward flow ($r < -0.7$) in the Ross Sea and northward flow ($r > 0.7$) in eastern-WAIS and the AP. This pattern matches the results of Emanuelsson et al. (2018), which propose that anticyclonic events over the ABS occurring when the ASL is weak are major drivers for PPT in the W-WAIS/Ross Sector.

Figure 3.14-D shows the relationship between meridional wind and PPT in Weddell Sector, pointing that cyclonic activity was responsible for advecting moisture to this area during 1900-2014. Positive (negative) correlations in WAIS/Ross Sea (Weddell Sea/AP)

suggest such circulation pattern. Turner et al. (2019) found a similar cyclonic activity pushing moisture into the Weddell Sea region.

The ASL longitudinal shifts determine which West Antarctic region preferentially receives moisture. It becomes evident when comparing V-wnd "versus" PPT in eastern-WAIS and the Weddell Sector (Figures 3.14 B and D): in E-WAIS/Amundsen Sector, the ASL is centered at 160° W and its eastern flank places over WAIS, whereas in the latter, its center is at 100° W with the northerly flow towards the Weddell Sea. The ASL has become deeper and migrated north-eastward in the last hundreds of years, favoring moisture flux over eastern-WAIS, AP, and the Weddell Sea (Thomas et al., 2015; Raphael et al., 2016; Turner et al., 2019).

3.5.2 500 hPa meridional wind changes

From 1900 to 1979, trends in meridional wind varied within ±0.3 (Figure 3.15-A). Over the Antarctic plateau, those were virtually null, matching with the absent variation of PPT in Figure 3.7-A. The most intense and significant (p-value < 0.05) positive V-wnd trend occurred from the Ross Sea towards the Pacific Ocean; Due to the enhanced northward atmospheric circulation, PPT dropped in this area (Figure 3.7-A; Thomas et al., 2017).

A significant (p-value < 0.05) and intense (0.3 m s^{-1} $decade^{-1}$) negative V-wnd trend appeared over the AP and eastern-WAIS, and may explain the large increase of PPT found in Figure 3.7-A and by Thomas et al. (2008). Similar negative V-wnd changes occurred in the Wilkes Coast, resulting in more rainfall (Figure 3.7-A). Overall, the PPT trends in the "B1980" period (1900-1979) match the spatial pattern of atmospheric circulation changes (Figures 3.7-A and 3.15-A).

Figure 3.15-A also reveals a substantial ASL deepening – positive/negative V-wnd trends over Ross Sea/AP –, which agrees with Raphael et al. (2016). Other than ASL, the V-wind trends resemble an intensified ZW3: three centers of enhanced southward flow (90° W, 45°E, and 140° E) alternating with three of northward flow (0°, 100° E, and 160°W; Irving & Simmonds, 2015).

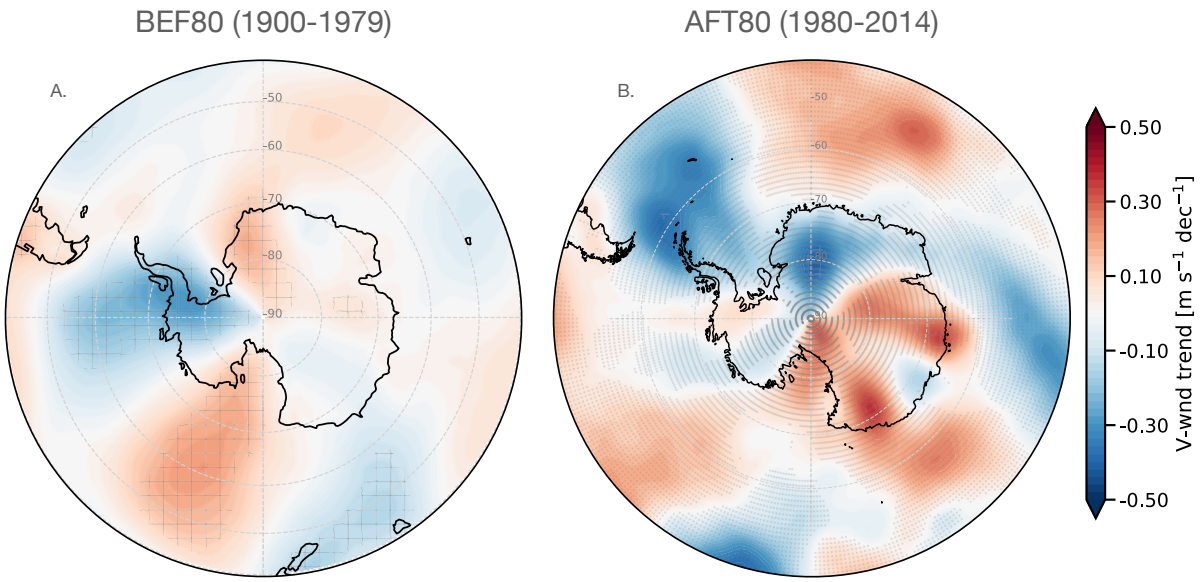

Figure 3.15: MRM7 V-wnd trend, in m s^{-1} decade^{-1}, during the periods (A) "B1980" (1900-1979) and (B) "A1980" (1980-2014). Red/blue shading attributes to enhanced northward/southward flow. Cross-hatching/stippling indicates where the trend/reanalyses agreement is significant at the 95% level.

An acceleration of V-wnd trends occurred during 1980-2014 compared to the first period (Figure 3.15-B), with values between ±0.5 m s^{-1} decade^{-1}. Despite large V-wnd trends, no significant (p-value $>$ 0.05) PPT changes developed in the Antarctic Plateau (Figure 3.7-B) – as there is virtually no moisture to be transported from inland to the coast, the intensified flow does not influence PPT. In coastal areas, however, V-wnd trends match PPT changes: less rainfall occurred in the George Coast, the Davis Sea, and in the Ross Sea, where southerly flow predominated; in Dronning Maud Land, Enderby Land, Wilkes Coast, northern AP, and the Weddell Sea, wetter conditions followed intensified southward winds (see locations in Figure 2.1). The enhanced southerly flow from inland to the Bellingshausen Sea resulted in negative PPT trends in south-western AP (Figure 3.7-B). Just as happened during "B1980", the spatial pattern of PPT trends and V-wnd trends also match in the latter period.

3.5.3 Climate indices

Once shown that PPT changes throughout 1900-2014 connect with the atmospheric circulation, we further explore its behavior through climate indices. As pointed in Chapter 1, the SAM (ZW3) positive phase relates to intensified zonal (meridional) circulation.

Despite V-wnd trends revealing an enhanced meridional circulation (Figure 3.15) – even suggesting a ZW3 spatial pattern – the ZW3 index (I_{ZW3}) showed no trends significantly different from zero (p-value > 0.1; Figure 3.16-B). Its negligible trend during "B1980" became closer to zero in the last period (from 5.2e-3 to 1e-3 decade^{-1}, respectively). Our findings for I_{ZW3} time series and trend manifested no direct connection with the PPT changes. Regardless, Marshall et al. (2017) discuss composites of PPT anomalies associated with ZW3 conditions; They found that its positive phase creates moisture paths towards the Wilkes Land, the Weddell Sea, and Enderby Land, plus drier conditions in western-WAIS and the Ross Sea. Our estimates of PPT changes (Figure 3.7) match such spatial patterns.

The SAM index (I_{SAM}) displayed high positive trends through the entire period analyzed (Figure 3.16-A). Particularly, its trend increased over 20% from 1900-1979 to 1980-2014: from 1.9e-2 to 2.3e-2 hPa decade^{-1}, with p-value < 0.01 in both. From 1900 to 1965, I_{SAM} was negative, suggesting a weaker circumpolar trough; it shifted to positive since 1965, accompanied by the westerlies' strengthening and migration southward (Marshall, 2007). Numerous studies ratify such I_{SAM} shift (Thompson & Wallace, 2000; Goodwin et al., 2016; Purich et al., 2016; IPCC, 2021). Marshall et al. (2017) established that the SAM relates to positive (negative) PPT anomalies over the AP (Antarctic Plateau); Medley & Thomas (2019) further detailed that the SAM is also responsible for the PPT dipole in the WAIS subregions, and attributed 80% of the snow accumulation spatial variability during 1957–2000 to its positive trend.

Beyond the SAM itself affecting the PPT spatial and temporal variability, it also plays a role in strengthening or dampening other climate phenomena: Wille et al. (2021), for example, discusses how the positive I_{SAM} trend intensifies the ASL deepening and

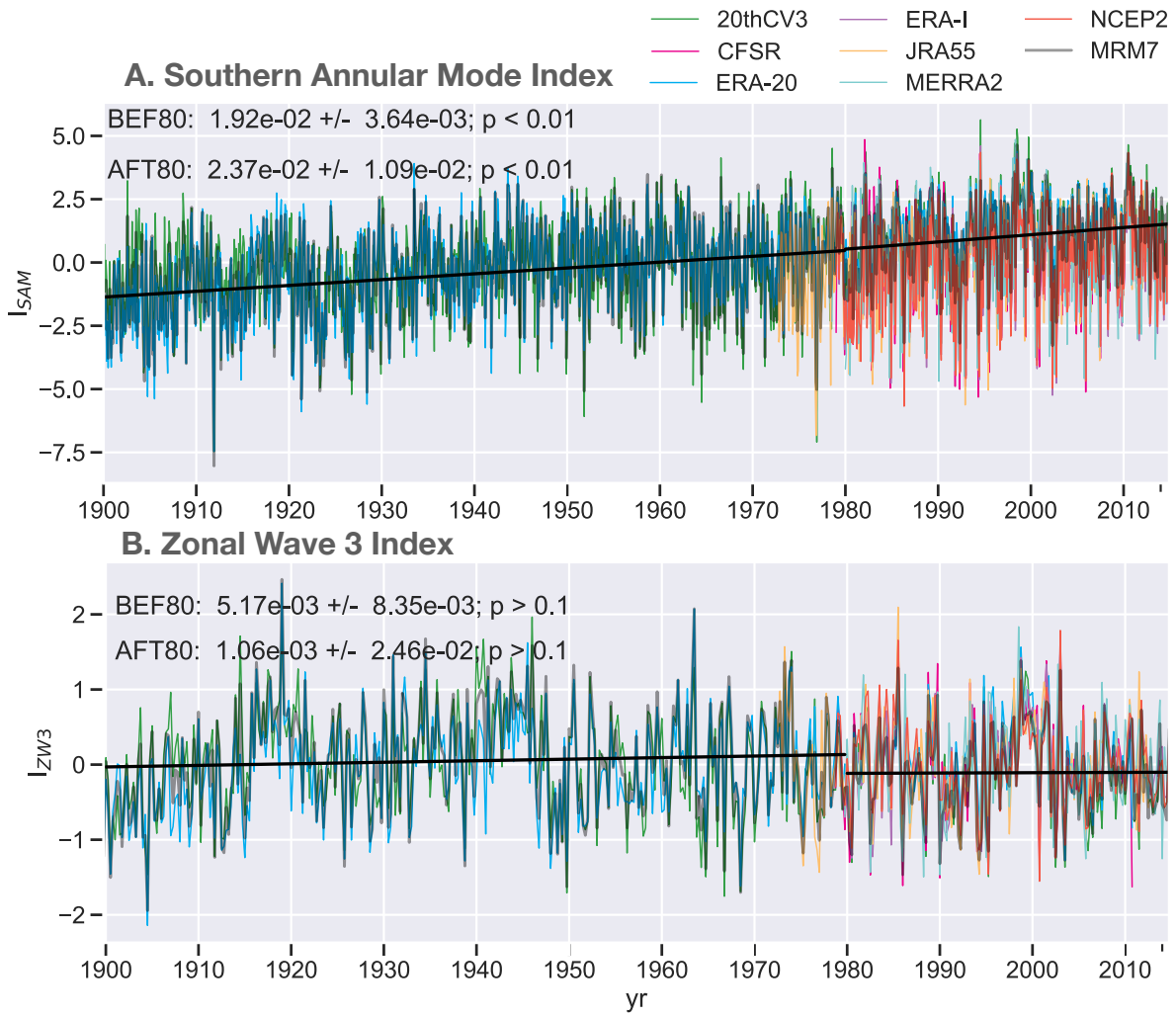

Figure 3.16: Temporal evolution of the (A) Southern Annular Mode Index and the (B) Zonal Wave Three Index. Colored lines show the indices for individual reanalyses and black for the MRM7. The black line and texts show the linear fit for both indices during "B1980" (1900-1979) and "A1980" (1980-2014).

migration north-eastwards, which, in turn, modifies PPT.

On top of that, Fyke et al. (2017) discusses the complexity of the Antarctic climate regarding the modes of variability: not only do they exert influence on precipitation, but their signals superimpose in a way that involves inter-mode interactions.

4 Summary and Conclusions

Precipitation in the Austral region (south of 60° S) underwent an overall increase between 1900 and 2014 – most rapidly from 1980 onwards – according to 23 CMIP6 models and seven reanalysis products. Yet, PPT trends were spatially inhomogeneous across the Antarctic Ice Sheet (AIS): while regions such as the Antarctic Peninsula and the Wilkes Coast experienced more rainfall, western-WAIS and the Ross Sea became drier (Figure 3.7). Fyke et al. (2017), Thomas et al. (2017), Medley & Thomas (2019) and other studies confirm such regional differences. Approaching PPT changes in the AIS through a regional perspective is essential since mass gains in one area may offset losses in another, masking a continental-wide signal; That is possibly the reason for studies as Monaghan et al. (2006), Bromwich et al. (2011), or Shepherd et al. (2012) reporting non-significant PPT changes in Antarctica in the last decades.

We addressed a transitional epoch in climate history, considering two periods: the first starting in the early industrial era (1900) and extending through 1979, and the latter spanning from 1980 to 2014. Our date milestone – the year 1979 – established the epoch when anthropogenic forcing (i.e., ozone depletion and GHG concentration increases) overcame the natural variability (Lenaerts et al., 2018; IPCC, 2021). The PPT trends in the averaged Austral region indeed showed a remarkable acceleration during 1980-2014 relative to 1900-1979; the rate grew 60% for the multi-reanalysis mean (MRM7) and sevenfold for the multi-model mean (MMM23; Figure 3.9). The regional estimates for both MRM7 and MMM23 exhibited larger rate values in the later period as well (Figure 3.9); Despite such rates progression, the values were negligible in EAIS, revealing unchanged PPT, and in W-WAIS/Ross Sector, they remained negative all along 1900-2014.

By comparing atmospheric-only models with coupled models, we showed that ocean-atmosphere feedbacks are fundamental in boosting precipitation (Figure 3.10); The temperature of the ocean's surface prompts evaporation that determines moisture content in

the air, which, in turn, controls the amount of precipitation over the AIS (Kittel et al., 2018). But variations in Southern Ocean SST contributed to only a discrete fraction in driving precipitation changes in the Austral region during 1900-2014, especially after 1980 when SST trends explained less than 5% of PPT trends (Figure 3.13).

Schneider et al. (2020) simulated the Antarctic precipitation response to the thermodynamical (surface temperature changes) and dynamical (atmospheric circulation changes) forcings in an ozone depletion scenario; They concluded that the primary mechanism driving PPT changes over the AIS were variations in the atmospheric circulation – particularly the circumpolar trough's migration poleward – rather than in the surface temperature. Accordingly, we found that the meridional wind at the 500 hPa level (V-wnd) was intimately linked to Austral precipitation since it exchanges moist air masses between Antarctica and northern areas. Regional Antarctic PPT was associated with southward flows pushed by atmospheric circulation features (Figure 3.12). For example, (1) the eastern flank of the Amundsen Sea Low (ASL) links eastern-WAIS and the Weddell Sea with moist air masses from the Pacific Ocean (Thomas et al., 2015), and (2) anticyclones over the Ross Sea, generally occurring when the ASL is weak, advect moisture from offshore to the western-WAIS (Emanuelsson et al., 2018). Consistent with Nicolas & Bromwich (2011b), we found an evident connection between PPT trends and V-wnd trends, as their spatial patterns match (Figures 3.7 and 3.15): areas with intensified southward/northward flow become wetter/drier. Beyond that, as V-wnd trends became more intense during 1980-2014 regarding 1900-1979, so did PPT changes.

We also addressed two climate modes important for high southern latitudes, the Southern Annular Mode (SAM) and the Zonal Wave 3 (ZW3). The ZW3 indicates the meridional flow intensity; Despite V-wnd trends suggesting stronger interactions between high and mid-latitudes, the ZW3 index revealed negligible changes (Figure 3.16-B). Our estimates for PPT trends are consistent with Marshall et al. (2017) with respect to the spatial distributions of PPT anomalies related to the ZW3 positive phase: drier western-WAIS and the Ross Sea, and more rainfall in the AP, the Weddell Sea, Wilkes Coast, and Enderby Land.

Contrary to the ZW3, SAM relates to a predominantly zonal flow around Antarctica that isolates the Austral climate from northern influences. In the late century, the positive phase of the SAM has been established and has undoubtedly strengthened since 1970 due to ozone depletion and GHG concentration increases (Figure 3.16-A; Thompson & Wallace, 2000; Lenaerts et al., 2018; IPCC, 2021); The SAM forces over 30% of the Austral climate (Marshall, 2007), therefore its variability directly implies PPT changes. Similar to our findings, Marshall et al. (2017) and Medley & Thomas (2019) discuss regional "SAM-congruent" PPT changes in which mass gains and losses balance on the Antarctic plateau and a dipole appears in WAIS – western/eastern region turns drier/wetter. Medley & Thomas (2019) further concluded, with high statistical confidence, that 80% of the snow accumulation variability across the WAIS during 1957-2000 was driven by the SAM index positive trends, thus, by changes in the atmosphere dynamics.

In this study, we tackled precipitation, which accounts for more than 90% of the surface mass balance over the AIS (Van Wessem et al., 2014) and has immediate implications on the global climate; In particular, since the AIS serves as the world's biggest water reservoir, its mass budget regulates the ice sheet's contribution to sea-level variations (Fyke et al., 2017; IPCC, 2021). Medley & Thomas (2019) calculated that mass input into the AIS mitigated the global mean sea-level rise at a rate of 1.12 ± 0.45 mm decade^{-1} between 1901 and 2000; Moreover, they showed that as PPT trends accelerated since 1980, so did the mitigation rate (2.47 ± 0.76 mm decade^{-1}). Note, the AIS has been and is currently contributing to the sea-level rise through melting (Shepherd et al., 2018; Shepherd et al., 2019 Kim et al., 2020; Smith et al., 2020); However, snow accumulation gains because of precipitation increases play a role in dampening total mass loss. In fact, Lenaerts et al. (2018) concluded that "Antarctic mass loss trends and associated sea-level contributions over 1992–2005 would have been approximately double (98 ± 21% larger) in the absence of ozone depletion-forced precipitation increases".

Regarding the CMIP6 models' performance, we conclude that precipitation is wet biased, consistent with Roussel et al. (2020), which further adds that no significant improvement was made from CMIP5 to CMIP6 regarding this issue. Palerme et al. (2017b)

and Roussel et al. (2020) suggest that the ocean-atmosphere feedbacks in the coupled models may be responsible for PPT being overestimated once the atmospheric-only models are closer to observations (also shown in Figure 3.10-A). Either way, the models were able to reproduce the PPT climatological 1900-2014 mean-field (Figure 3.3) and the seasonal cycle (Figure 3.5). The time series showed that the multi-reanalysis mean (our reference value) placed within the multi-model mean (MMM23) 95% confidence interval, despite the latter overestimating PPT throughout 1900-2014 (Figure 3.8). MMM23 captured the overall precipitation changes in the Austral region – spatial large-scale pattern and acceleration after 1980 –, though with more discrete values (Figure 3.9); But, it was unable to reproduce regional differences of PPT trends inland Antarctica, which are crucial for global climate implications as discussed previously.

Palerme et al. (2017b) noted that sea surface conditions bias in coupled models affects PPT outputs over the Austral region. That is a major problem, considering that the CMIP6 models failed to reproduce SST changes after 1980 (Figure 3.11; IPCC, 2021). Purich et al. (2016) discusses that coupled models underestimate the westerly jet strengthening under the current (since ≈1970) scenario of ozone depletion and GHG concentration increases; Because of that, they minimize the Ekman transport equatorward that spreads Antarctic cold water to the north and results in negative SST trends. Another hypothesis for the CMIP6 improper SST changes are cloud-related shortwave biases, as discussed in Hyder et al. (2018) and Wang et al. (2021a).

Antarctica and the Southern Ocean lack observations; Therefore, we proposed to overcome such obstacle by assessing reanalysis and numerical models products. To reduce uncertainties of individual products, we used ensembles for both data types, precisely their means, which enhances the statistical confidence in our analyses (Tebaldi & Knutti, 2007; Maher et al., 2021); In fact, Figure 3.1 showed the multi-model mean closest to our reference value – the multi-reanalysis mean – than individual CMIP6 models. We further measured the statistical significance of our "multi-datasets" analyses through model agreement, as in Pontes et al. (2020).

Precipitation in the Austral region has increased since 1900, much more abruptly since

the decade 1970, and might be related to human activities forcing the climate (IPCC, 2021). Projections suggest that the Antarctic Ice Sheet will continue to gain mass under warmer conditions, which can contribute to dampening the losses through melting and consequent sea-level rise (Frieler et al., 2015; Palerme et al., 2017b; Lenaerts et al., 2018; Rodehacke et al., 2020). In order to improve the projections and our understanding of the Antarctic and global climate, further studies must be carried with high-quantity and high-quality observational data and advanced coupled models. The Southern Ocean contribution to precipitation changes demands extra investigation, possibly following improvement in the global climate models, and also an examination considering changes in the deep-ocean dynamics and thermodynamics.

Bibliography

Agresti, A., 1990. Categorical Data Analysis, chapter 4.

Allison, I., Alley, R. B., Fricker, H., Thomas, R., Warner, R., 2009. Ice sheet mass balance and sea level. Antarctic Science 21 (5), 413–426.

Armour, K. C., Marshall, J., Scott, J. R., Donohoe, A., Newsom, E. R., 2016. Southern Ocean warming delayed by circumpolar upwelling and equatorward transport. Nature Geoscience 9 (7), 549–554.

Auger, M., Morrow, R., Kestenare, E., Sallée, J.-B., Cowley, R., 2021. Southern Ocean in-situ temperature trends over 25 years emerge from interannual variability. Nature Communications 12 (1), 1–9.

Bao, Y., Song, Z., Qiao, F., 2020. FIO-ESM version 2.0: Model description and evaluation. Journal of Geophysical Research: Oceans 125 (6), e2019JC016036.

Beadling, R., Russell, J., Stouffer, R., Mazloff, M., Talley, L., Goodman, P., Sallée, J.-B., Hewitt, H., Hyder, P., Pandde, A., 2020. Representation of Southern Ocean properties across coupled model intercomparison project generations: CMIP3 to CMIP6. Journal of Climate 33 (15), 6555–6581.

Behrangi, A., Christensen, M., Richardson, M., Lebsock, M., Stephens, G., Huffman, G. J., Bolvin, D., Adler, R. F., Gardner, A., Lambrigtsen, B., et al., 2016. Status of high-latitude precipitation estimates from observations and reanalyses. Journal of Geophysical Research: Atmospheres 121 (9), 4468–4486.

Bosilovich, M., Cullather, R., for Atmospheric Research Staff (Eds), N. C., 2019. The Climate Data Guide: NASA's MERRA2 reanalysis.
URL `https://climatedataguide.ucar.edu/climate-data/nasas-merra2-reanalysis`

Bosilovich, M., Lucchesi, R., Suarez, M., 2015. MERRA-2: File specification.

Bozkurt, D., Bromwich, D. H., Carrasco, J., Rondanelli, R., 2021. Temperature and precipitation projections for the Antarctic Peninsula over the next two decades: contrasting global and regional climate model simulations. Climate Dynamics 56 (11), 3853–3874.

Bracegirdle, T., Holmes, C., Hosking, J., Marshall, G., Osman, M., Patterson, M., Rackow, T., 2020. Improvements in circumpolar southern hemisphere extratropical atmospheric circulation in CMIP6 Compared to CMIP5. Earth and Space Science 7 (6), e2019EA001065.

Bracegirdle, T. J., Colleoni, F., Abram, N. J., Bertler, N. A., Dixon, D. A., England, M., Favier, V., Fogwill, C. J., Fyfe, J. C., Goodwin, I., et al., 2019. Back to the future: Using long-term observational and paleo-proxy reconstructions to improve model projections of Antarctic climate. Geosciences 9 (6), 255.

Bromwich, D. H., Nicolas, J. P., Monaghan, A. J., 2011. An assessment of precipitation changes over Antarctica and the Southern Ocean since 1989 in contemporary global reanalyses. Journal of Climate 24 (16), 4189–4209.

Cao, J., Wang, B., Yang, Y.-M., Ma, L., Li, J., Sun, B., Bao, Y., He, J., Zhou, X., Wu, L., 2018. The NUIST Earth System Model (NESM) version 3: description and preliminary evaluation. Geoscientific Model Development 11 (7), 2975–2993.

Cherchi, A., Fogli, P. G., Lovato, T., Peano, D., Iovino, D., Gualdi, S., Masina, S., Scoccimarro, E., Materia, S., Bellucci, A., et al., 2019. Global mean climate and main patterns of variability in the CMCC-CM2 coupled model. Journal of Advances in Modeling Earth Systems 11 (1), 185–209.

Clark, P. U., Alley, R. B., Pollard, D., 1999. Northern Hemisphere ice-sheet influences on global climate change. Science 286 (5442), 1104–1111.

Dalaiden, Q., Goosse, H., Klein, F., Lenaerts, J., Holloway, M., Sime, L., Thomas, E. R., 2019. Surface Mass Balance of the Antarctic Ice Sheet and its link with surface temperature change in model simulations and reconstructions. The Cryosphere Discussions.

Dee, D., Uppala, S., 2008. Variational bias correction in ERA-Interim.

Delaygue, G., Masson, V., Jouzel, J., Koster, R. D., Healy, R. J., 2000. The origin of Antarctic precipitation: a modelling approach. Tellus B 52 (1), 19–36.

Dick, D., 2019. The Climate Data Guide: ERA-Interim.
URL `https://climatedataguide.ucar.edu/climate-data/era-interim`

Doddridge, E. W., Marshall, J., Song, H., Campin, J.-M., Kelley, M., Nazarenko, L., 2019. Eddy compensation dampens Southern Ocean sea surface temperature response to westerly wind trends. Geophysical Research Letters 46 (8), 4365–4377.

Donat-Magnin, M., Jourdain, N. C., Gallée, H., Amory, C., Kittel, C., Fettweis, X., Wille, J. D., Favier, V., Drira, A., Agosta, C., 2020. Interannual variability of summer surface mass balance and surface melting in the Amundsen sector, West Antarctica. The Cryosphere 14 (1), 229–249.

Eisen, O., Frezzotti, M., Genthon, C., Isaksson, E., Magand, O., Van Den Broeke, M. R., Dixon, D. A., Ekaykin, A., Holmlund, P., Kameda, T., et al., 2008. Ground-based measurements of spatial and temporal variability of snow accumulation in East Antarctica. Reviews of Geophysics 46 (2).

Emanuelsson, B. D., Bertler, N. A., Neff, P. D., Renwick, J. A., Markle, B. R., Baisden, W. T., Keller, E. D., 2018. The role of Amundsen–Bellingshausen Sea anticyclonic circulation in forcing marine air intrusions into West Antarctica. Climate Dynamics 51 (9), 3579–3596.

Eyring, V., Bony, S., Meehl, G. A., Senior, C. A., Stevens, B., Stouffer, R. J., Taylor, K. E., 2016. Overview of the Coupled Model Intercomparison Project Phase 6 (CMIP6)

experimental design and organization. Geoscientific Model Development 9 (5), 1937–1958.

Ferrero, B., Tonelli, M., Marcello, F., Wainer, I., 2021. Long-term regional dynamic sea level changes from CMIP6 projections. Advances in Atmospheric Sciences 38 (2), 157–167.

Fligner, M. A., Policello, G. E., 1981. Robust rank procedures for the Behrens-Fisher problem. Journal of the American Statistical Association 76 (373), 162–168.

Frieler, K., Clark, P. U., He, F., Buizert, C., Reese, R., Ligtenberg, S. R., Van Den Broeke, M. R., Winkelmann, R., Levermann, A., 2015. Consistent evidence of increasing Antarctic accumulation with warming. Nature Climate Change 5 (4), 348–352.

Fyke, J., Lenaerts, J., Wang, H., 2017. Basin-scale heterogeneity in Antarctic precipitation and its impact on surface mass variability. The Cryosphere 11 (6), 2595–2609.

Gille, S. T., 2008. Decadal-scale temperature trends in the Southern Hemisphere ocean. Journal of Climate 21 (18), 4749–4765.

Golaz, J.-C., Caldwell, P. M., Van Roekel, L. P., Petersen, M. R., Tang, Q., Wolfe, J. D., Abeshu, G., Anantharaj, V., Asay-Davis, X. S., Bader, D. C., et al., 2019. The DOE E3SM coupled model version 1: Overview and evaluation at standard resolution. Journal of Advances in Modeling Earth Systems 11 (7), 2089–2129.

Gong, D., Wang, S., 1999. Definition of Antarctic oscillation index. Geophysical research letters 26 (4), 459–462.

Goodwin, B. P., Mosley-Thompson, E., Wilson, A. B., Porter, S. E., Sierra-Hernandez, M. R., 2016. Accumulation variability in the Antarctic Peninsula: The role of large-scale atmospheric oscillations and their interactions. Journal of Climate 29 (7), 2579–2596.

Goodwin, I., De Angelis, M., Pook, M., Young, N., 2003. Snow accumulation variability in Wilkes Land, East Antarctica, and the relationship to atmospheric ridging in the 130–170 E region since 1930. Journal of Geophysical Research: Atmospheres 108 (D21).

Gourieroux, C., Holly, A., Monfort, A., 1982. Likelihood ratio test, Wald test, and Kuhn-Tucker test in linear models with inequality constraints on the regression parameters. Econometrica: journal of the Econometric Society, 63–80.

Hajima, T., Watanabe, M., Yamamoto, A., Tatebe, H., Noguchi, M. A., Abe, M., Ohgaito, R., Ito, A., Yamazaki, D., Okajima, H., et al., 2020. Development of the MIROC-ES2L Earth system model and the evaluation of biogeochemical processes and feedbacks. Geoscientific Model Development 13 (5), 2197–2244.

Hall, A., Visbeck, M., 2002. Synchronous variability in the Southern Hemisphere atmosphere, sea ice, and ocean resulting from the annular mode. Journal of Climate 15 (21), 3043–3057.

Hanna, E., Navarro, F. J., Pattyn, F., Domingues, C. M., Fettweis, X., Ivins, E. R., Nicholls, R. J., Ritz, C., Smith, B., Tulaczyk, S., et al., 2013. Ice-sheet mass balance and climate change. Nature 498 (7452), 51–59.

Huang, B., Thorne, P. W., Banzon, V. F., Boyer, T., Chepurin, G., Lawrimore, J. H., Menne, M. J., Smith, T. M., Vose, R. S., Zhang, H.-M., 2017. Extended reconstructed sea surface temperature, version 5 (ERSSTv5): upgrades, validations, and intercomparisons. Journal of Climate 30 (20), 8179–8205.

Hyder, P., Edwards, J. M., Allan, R. P., Hewitt, H. T., Bracegirdle, T. J., Gregory, J. M., Wood, R. A., Meijers, A. J., Mulcahy, J., Field, P., et al., 2018. Critical Southern Ocean climate model biases traced to atmospheric model cloud errors. Nature communications 9 (1), 1–17.

IPCC, 2021. "Climate Change 2021: The Physical Science Basis". The Working Group I contribution to the IPCC's Sixth Assessment Report (AR6).
URL https://www.ipcc.ch/2021/08/09/ar6-wg1-20210809-pr/

Irving, D., Simmonds, I., 2015. A novel approach to diagnosing Southern Hemisphere planetary wave activity and its influence on regional climate variability. Journal of Climate 28 (23), 9041–9057.

Jones, J. M., Gille, S. T., Goosse, H., Abram, N. J., Canziani, P. O., Charman, D. J., Clem, K. R., Crosta, X., de Lavergne, C., Eisenman, I., et al., 2016. Assessing recent trends in high-latitude Southern Hemisphere surface climate. Nature Climate Change 6 (10), 917–926.

Jungclaus, J., Bard, E., Baroni, M., Braconnot, P., Cao, J., Chini, L., Egorova, T., Evans, M., González-Rouco, J. F., Goosse, H., et al., 2017. The PMIP4 contribution to CMIP6–Part 3: The last millennium, scientific objective, and experimental design for the PMIP4 past1000 simulations.

Kanamitsu, M., Ebisuzaki, W., Woollen, J., Yang, S.-K., Hnilo, J., Fiorino, M., Potter, G., 2002. NCEP/DOE AMIP-II Reanalysis (R-2). Bulletin of the American Meteorological Society 83 (11), 1631–1644.

Kelley, M., Schmidt, G. A., Nazarenko, L. S., Bauer, S. E., Ruedy, R., Russell, G. L., Ackerman, A. S., Aleinov, I., Bauer, M., Bleck, R., et al., 2020. GISS-E2. 1: Configurations and climatology. Journal of Advances in Modeling Earth Systems 12 (8), e2019MS002025.

Kim, B.-H., Seo, K.-W., Eom, J., Chen, J., Wilson, C. R., 2020. Antarctic ice mass variations from 1979 to 2017 driven by anomalous precipitation accumulation. Scientific reports 10 (1), 1–9.

Kittel, C., Amory, C., Agosta, C., Delhasse, A., Doutreloup, S., Huot, P.-V., Wyard, C., Fichefet, T., Fettweis, X., 2018. Sensitivity of the current Antarctic surface mass balance to sea surface conditions using MAR. The Cryosphere 12 (12), 3827–3839.

Kobayashi, S., Ota, Y., Harada, Y., Ebita, A., Moriya, M., Onoda, H., Onogi, K., Kamahori, H., Kobayashi, C., Endo, H., et al., 2015. The JRA-55 reanalysis: General specifications and basic characteristics. Journal of the Meteorological Society of Japan. Ser. II 93 (1), 5–48.

Kostov, Y., Ferreira, D., Armour, K. C., Marshall, J., 2018. Contributions of greenhouse

gas forcing and the Southern Annular Mode to historical Southern Ocean surface temperature trends. Geophysical Research Letters 45 (2), 1086–1097.

Krinner, G., Magand, O., Simmonds, I., Genthon, C., Dufresne, J.-L., 2007. Simulated Antarctic precipitation and surface mass balance at the end of the twentieth and twenty-first centuries. Climate Dynamics 28 (2-3), 215–230.

Krishnan, R., Swapna, P., Choudhury, A. D., Narayansetti, S., Prajeesh, A., Singh, M., Modi, A., Mathew, R., Vellore, R., Jyoti, J., et al., 2021. The IITM Earth System Model (IITM ESM). arXiv preprint arXiv:2101.03410.

Lauritzen, P. H., Nair, R. D., Herrington, A., Callaghan, P., Goldhaber, S., Dennis, J., Bacmeister, J., Eaton, B., Zarzycki, C., Taylor, M. A., et al., 2018. NCAR release of CAM-SE in CESM2. 0: A reformulation of the spectral element dynamical core in dry-mass vertical coordinates with comprehensive treatment of condensates and energy. Journal of Advances in Modeling Earth Systems 10 (7), 1537–1570.

Lee Rodgers, J., Nicewander, W. A., 1988. Thirteen ways to look at the correlation coefficient. The American Statistician 42 (1), 59–66.

Lenaerts, J. T., Fyke, J., Medley, B., 2018. The signature of ozone depletion in recent Antarctic precipitation change: A study with the Community Earth System Model. Geophysical Research Letters 45 (23), 12–931.

Lenaerts, J. T., van Meijgaard, E., van den Broeke, M. R., Ligtenberg, S. R., Horwath, M., Isaksson, E., 2013. Recent snowfall anomalies in Dronning Maud Land, East Antarctica, in a historical and future climate perspective. Geophysical Research Letters 40 (11), 2684–2688.

Li, L., Yu, Y., Tang, Y., Lin, P., Xie, J., Song, M., Dong, L., Zhou, T., Liu, L., Wang, L., et al., 2020. The flexible global ocean-atmosphere-land system model grid-point version 3 (fgoals-g3): description and evaluation. Journal of Advances in Modeling Earth Systems 12 (9), e2019MS002012.

Li, X., Cai, W., Meehl, G. A., Chen, D., Yuan, X., Raphael, M., Holland, D. M., Ding, Q., Fogt, R. L., Markle, B. R., et al., 2021. Tropical teleconnection impacts on Antarctic climate changes. Nature Reviews Earth & Environment, 1–19.

Lurton, T., Balkanski, Y., Bastrikov, V., Bekki, S., Bopp, L., Braconnot, P., Brockmann, P., Cadule, P., Contoux, C., Cozic, A., et al., 2020. CMIP6 forcing data as implemented in the IPSL-CM6 model. J. Adv. Model. Earth Syst 12, e2019MS001940.

Maher, N., Milinski, S., Ludwig, R., 2021. Large ensemble climate model simulations: introduction, overview, and future prospects for utilising multiple types of large ensemble. Earth System Dynamics 12 (2), 401–418.

Marshall, G. J., 2003. Trends in the Southern Annular Mode from observations and reanalyses. Journal of climate 16 (24), 4134–4143.

Marshall, G. J., 2007. Half-century seasonal relationships between the Southern Annular Mode and Antarctic temperatures. International Journal of Climatology: A Journal of the Royal Meteorological Society 27 (3), 373–383.

Marshall, G. J., Thompson, D. W., van den Broeke, M. R., 2017. The signature of Southern Hemisphere atmospheric circulation patterns in Antarctic precipitation. Geophysical Research Letters 44 (22), 11–580.

Mauritsen, T., Bader, J., Becker, T., Behrens, J., Bittner, M., Brokopf, R., Brovkin, V., Claussen, M., Crueger, T., Esch, M., et al., 2019. Developments in the MPI-M Earth System Model version 1.2 (MPI-ESM1. 2) and its response to increasing CO2. Journal of Advances in Modeling Earth Systems 11 (4), 998–1038.

Medley, B., Thomas, E., 2019. Increased snowfall over the Antarctic Ice Sheet mitigated twentieth-century sea-level rise. Nature Climate Change 9 (1), 34–39.

Milinski, S., Maher, N., Olonscheck, D., 2020. How large does a large ensemble need to be? Earth System Dynamics 11 (4), 885–901.

Monaghan, A. J., Bromwich, D. H., Fogt, R. L., Wang, S.-H., Mayewski, P. A., Dixon, D. A., Ekaykin, A., Frezzotti, M., Goodwin, I., Isaksson, E., et al., 2006. Insignificant change in Antarctic snowfall since the IGY. Science 313 (5788), 827–831.

NCAR Staff Online, E., 2017. The Climate Data Guide: Climate Forecast System Reanalysis (CFSR).
URL https://climatedataguide.ucar.edu/climate-data/climate-forecast-system-reanalysis-cfsr

Nicolas, J. P., Bromwich, D. H., 2011a. Climate of West Antarctica and influence of marine air intrusions. Journal of Climate 24 (1), 49–67.

Nicolas, J. P., Bromwich, D. H., 2011b. Precipitation changes in high southern latitudes from global reanalyses: A cautionary tale. Surveys in geophysics 32 (4-5), 475–494.

Palerme, C., Claud, C., Dufour, A., Genthon, C., Wood, N. B., L'Ecuyer, T., 2017a. Evaluation of Antarctic snowfall in global meteorological reanalyses. Atmospheric Research 190, 104–112.

Palerme, C., Genthon, C., Claud, C., Kay, J. E., Wood, N. B., LEcuyer, T., 2017b. Evaluation of current and projected Antarctic precipitation in CMIP5 models. Climate dynamics 48 (1-2), 225–239.

Philippe, M., Tison, J.-L., Fjøsne, K., Hubbard, B., Kjær, H. A., Lenaerts, J., Drews, R., Sheldon, S. G., Bondt, K. D., Claeys, P., et al., 2016. Ice core evidence for a 20th century increase in surface mass balance in coastal Dronning Maud Land, East Antarctica. The Cryosphere 10 (5), 2501–2516.

Poli, P., Hersbach, H., Dee, D. P., Berrisford, P., Simmons, A. J., Vitart, F., Laloyaux, P., Tan, D. G., Peubey, C., Thépaut, J.-N., et al., 2016. ERA-20C: An atmospheric reanalysis of the twentieth century. Journal of Climate 29 (11), 4083–4097.

Poli, P. . N. C. f. A. R. S. E., 2017. The Climate Data Guide: ERA-20C: ECMWF's atmospheric reanalysis of the 20th century (and comparisons with NOAA's 20CR).

URL https://climatedataguide.ucar.edu/climate-data/era-20c-ecmwfs-atmospheric-reanalysis-20th-century-and-comparisons-noaas-20cr

Pontes, G., Wainer, I., Prado, L., Brierley, C., 2020. Reduced Atlantic variability in the mid-Pliocene. Climatic Change 160 (3), 445–461.

Purich, A., Cai, W., England, M. H., Cowan, T., 2016. Evidence for link between modelled trends in Antarctic sea ice and underestimated westerly wind changes. Nature communications 7 (1), 1–9.

Purich, A., England, M. H., Cai, W., Sullivan, A., Durack, P. J., 2018. Impacts of broad-scale surface freshening of the southern ocean in a coupled climate model. Journal of Climate 31 (7), 2613–2632.

Raphael, M. N., 2004. A zonal wave 3 index for the Southern Hemisphere. Geophysical Research Letters 31 (23).

Raphael, M. N., Marshall, G., Turner, J., Fogt, R., Schneider, D., Dixon, D., Hosking, J., Jones, J., Hobbs, W. R., 2016. The Amundsen Sea low: Variability, change, and impact on Antarctic climate. Bulletin of the American Meteorological Society 97 (1), 111–121.

Roberts, J., Plummer, C., Vance, T., van Ommen, T., Moy, A., Poynter, S., Treverrow, A., Curran, M., George, S., 2014. A two thousand year annual record of snow accumulation rates for Law Dome, East Antarctica. Climate of the Past Discussions 10, 4469–4497.

Rodehacke, C. B., Pfeiffer, M., Semmler, T., Gurses, Ö., Kleiner, T., 2020. Future sea level contribution from Antarctica inferred from CMIP5 model forcing and its dependence on precipitation ansatz. Earth System Dynamics 11 (4), 1153–1194.

Rong, X., Li, J., Chen, H., Xin, Y., Su, J., Hua, L., Zhou, T., Qi, Y., Zhang, Z., Zhang, G., et al., 2018. The CAMS climate system model and a basic evaluation of its climatology and climate variability simulation. Journal of Meteorological Research 32 (6), 839–861.

Roussel, M.-L., Lemonnier, F., Genthon, C., Krinner, G., 2020. Brief communication: Evaluating Antarctic precipitation in ERA5 and CMIP6 against CloudSat observations. The Cryosphere 14 (8), 2715–2727.

Saha, S., Moorthi, S., Pan, H.-L., Wu, X., Wang, J., Nadiga, S., Tripp, P., Kistler, R., Woollen, J., Behringer, D., et al., 2010. The NCEP climate forecast system reanalysis. Bulletin of the American Meteorological Society 91 (8), 1015–1058.

Schlosser, E., Haumann, F. A., Raphael, M. N., 2018. Atmospheric influences on the anomalous 2016 Antarctic sea ice decay. The Cryosphere 12 (3), 1103–1119.

Schlosser, E., Stenni, B., Valt, M., Cagnati, A., Powers, J. G., Manning, K. W., Raphael, M., Duda, M. G., 2016. Precipitation and synoptic regime in two extreme years 2009 and 2010 at Dome C, Antarctica-implications for ice core interpretation. Atmospheric Chemistry & Physics 16 (8).

Schneider, D. P., Deser, C., Fan, T., 2015. Comparing the impacts of tropical SST variability and polar stratospheric ozone loss on the Southern Ocean westerly winds. Journal of Climate 28 (23), 9350–9372.

Schneider, D. P., Kay, J. E., Lenaerts, J., 2020. Improved clouds over southern ocean amplify antarctic precipitation response to ozone depletion in an earth system model. Climate Dynamics 55 (5), 1665–1684.

Seland, Ø., Bentsen, M., Olivié, D., Toniazzo, T., Gjermundsen, A., Graff, L. S., Debernard, J. B., Gupta, A. K., He, Y.-C., Kirkevåg, A., et al., 2020. Overview of the Norwegian Earth System Model (NorESM2) and key climate response of CMIP6 DECK, historical, and scenario simulations. Geoscientific Model Development 13 (12), 6165–6200.

Sellar, A. A., Jones, C. G., Mulcahy, J. P., Tang, Y., Yool, A., Wiltshire, A., O'connor, F. M., Stringer, M., Hill, R., Palmieri, J., et al., 2019. UKESM1: Description and evaluation of the UK Earth System Model. Journal of Advances in Modeling Earth Systems 11 (12), 4513–4558.

Semenov, M. A., Stratonovitch, P., 2010. Use of multi-model ensembles from global climate models for assessment of climate change impacts. Climate research 41 (1), 1–14.

Shepherd, A., Gilbert, L., Muir, A. S., Konrad, H., McMillan, M., Slater, T., Briggs, K. H., Sundal, A. V., Hogg, A. E., Engdahl, M. E., 2019. Trends in antarctic ice sheet elevation and mass. Geophysical Research Letters 46 (14), 8174–8183.

Shepherd, A., Ivins, E., Rignot, E., Smith, B., Van Den Broeke, M., Velicogna, I., Whitehouse, P., Briggs, K., Joughin, I., Krinner, G., et al., 2018. Mass balance of the antarctic ice sheet from 1992 to 2017. Nature 558, 219–222.

Shepherd, A., Ivins, E. R., Geruo, A., Barletta, V. R., Bentley, M. J., Bettadpur, S., Briggs, K. H., Bromwich, D. H., Forsberg, R., Galin, N., et al., 2012. A reconciled estimate of ice-sheet mass balance. Science 338 (6111), 1183–1189.

Simmons, A., 2006. ERA-Interim: New ECMWF reanalysis products from 1989 onwards. ECMWF newsletter 110, 25–36.

Sinclair, V., Dacre, H., 2019. Which extratropical cyclones contribute most to the transport of moisture in the Southern Hemisphere? Journal of Geophysical Research: Atmospheres 124 (5), 2525–2545.

Slater, T., Hogg, A. E., Mottram, R., 2020. Ice-sheet losses track high-end sea-level rise projections. Nature Climate Change 10 (10), 879–881.

Slivinski, L. C., Compo, G. P., Whitaker, J. S., Sardeshmukh, P. D., Giese, B. S., McColl, C., Allan, R., Yin, X., Vose, R., Titchner, H., et al., 2019. Towards a more reliable historical reanalysis: Improvements for version 3 of the Twentieth Century Reanalysis system. Quarterly Journal of the Royal Meteorological Society 145 (724), 2876–2908.

Smith, B., Fricker, H. A., Gardner, A. S., Medley, B., Nilsson, J., Paolo, F. S., Holschuh, N., Adusumilli, S., Brunt, K., Csatho, B., et al., 2020. Pervasive ice sheet mass loss reflects competing ocean and atmosphere processes. Science 368 (6496), 1239–1242.

Spence, P., Griffies, S. M., England, M. H., Hogg, A. M., Saenko, O. A., Jourdain, N. C., 2014. Rapid subsurface warming and circulation changes of Antarctic coastal waters by poleward shifting winds. Geophysical Research Letters 41 (13), 4601–4610.

Stenni, B., Curran, M. A., Abram, N., Orsi, A., Goursaud, S., Masson-Delmotte, V., Neukom, R., Goosse, H., Divine, D., Van Ommen, T., et al., 2017. Antarctic climate variability on regional and continental scales over the last 2000 years. Climate of the Past 13 (11), 1609–1634.

Sun, Q., Miao, C., Duan, Q., Ashouri, H., Sorooshian, S., Hsu, K.-L., 2018. A review of global precipitation data sets: Data sources, estimation, and intercomparisons. Reviews of Geophysics 56 (1), 79–107.

Swart, N. C., Cole, J. N., Kharin, V. V., Lazare, M., Scinocca, J. F., Gillett, N. P., Anstey, J., Arora, V., Christian, J. R., Hanna, S., et al., 2019. The Canadian earth system model version 5 (CanESM5. 0.3). Geoscientific Model Development 12 (11), 4823–4873.

Swart, N. C., Gille, S. T., Fyfe, J. C., Gillett, N. P., 2018. Recent Southern Ocean warming and freshening driven by greenhouse gas emissions and ozone depletion. Nature Geoscience 11 (11), 836–841.

Tang, M. S., Chenoli, S. N., Samah, A. A., Hai, O. S., 2018. An assessment of historical Antarctic precipitation and temperature trend using CMIP5 models and reanalysis datasets. Polar Science 15, 1–12.

Taylor, K. E., 2001. Summarizing multiple aspects of model performance in a single diagram. Journal of Geophysical Research: Atmospheres 106 (D7), 7183–7192.

Taylor, K. E., 2005. Taylor diagram primer. Work. Pap, 1–4.

Taylor, K. E., Stouffer, R. J., Meehl, G. A., 2012. An overview of CMIP5 and the experiment design. Bulletin of the American meteorological Society 93 (4), 485–498.

Tebaldi, C., Knutti, R., 2007. The use of the multi-model ensemble in probabilistic climate projections. Philosophical transactions of the royal society A: mathematical, physical and engineering sciences 365 (1857), 2053–2075.

Thomas, E. R., Hosking, J. S., Tuckwell, R. R., Warren, R., Ludlow, E., 2015. Twentieth century increase in snowfall in coastal West Antarctica. Geophysical Research Letters 42 (21), 9387–9393.

Thomas, E. R., Marshall, G. J., McConnell, J. R., 2008. A doubling in snow accumulation in the western Antarctic Peninsula since 1850. Geophysical research letters 35 (1).

Thomas, E. R., Melchior Van Wessem, J., Roberts, J., Isaksson, E., Schlosser, E., Fudge, T. J., Vallelonga, P., Medley, B., Lenaerts, J., Bertler, N., et al., 2017. Regional Antarctic snow accumulation over the past 1000 years. Climate of the Past 13 (11), 1491–1513.

Thompson, D. W., Wallace, J. M., 2000. Annular modes in the extratropical circulation. Part I: Month-to-month variability. Journal of climate 13 (5), 1000–1016.

Trenberth, K. E., 2011. Changes in precipitation with climate change. Climate Research 47 (1-2), 123–138.

Trenberth, K. E., Fasullo, J., Smith, L., 2005. Trends and variability in column-integrated atmospheric water vapor. Climate dynamics 24 (7), 741–758.

Turner, J., Colwell, S. R., Marshall, G. J., Lachlan-Cope, T. A., Carleton, A. M., Jones, P. D., Lagun, V., Reid, P. A., Iagovkina, S., 2005. Antarctic climate change during the last 50 years. International journal of Climatology 25 (3), 279–294.

Turner, J., Phillips, T., Hosking, J. S., Marshall, G. J., Orr, A., 2013. The Amundsen Sea low. International Journal of Climatology 33 (7), 1818–1829.

Turner, J., Phillips, T., Thamban, M., Rahaman, W., Marshall, G. J., Wille, J. D., Favier, V., Winton, V. H. L., Thomas, E., Wang, Z., et al., 2019. The dominant role of extreme precipitation events in Antarctic snowfall variability. Geophysical Research Letters 46 (6), 3502–3511.

Van de Berg, W., Van den Broeke, M., Reijmer, C., Van Meijgaard, E., 2005. Characteristics of the Antarctic surface mass balance, 1958–2002, using a regional atmospheric climate model. Annals of Glaciology 41, 97–104.

Van Wessem, J., Reijmer, C., Morlighem, M., Mouginot, J., Rignot, E., Medley, B., Joughin, I., Wouters, B., Depoorter, M., Bamber, J., et al., 2014. Improved representation of East Antarctic surface mass balance in a regional atmospheric climate model. Journal of Glaciology 60 (222), 761–770.

Van Wessem, J. M., Jan Van De Berg, W., Noël, B. P., Van Meijgaard, E., Amory, C., Birnbaum, G., Jakobs, C. L., Krüger, K., Lenaerts, J., Lhermitte, S., et al., 2018. Modelling the climate and surface mass balance of polar ice sheets using racmo2: Part 2: Antarctica (1979-2016). Cryosphere 12 (4), 1479–1498.

Velicogna, I., Wahr, J., 2006. Measurements of time-variable gravity show mass loss in Antarctica. science 311 (5768), 1754–1756.

Voldoire, A., Saint-Martin, D., Sénési, S., Decharme, B., Alias, A., Chevallier, M., Colin, J., Guérémy, J.-F., Michou, M., Moine, M.-P., et al., 2019. Evaluation of CMIP6 deck experiments with CNRM-CM6-1. Journal of Advances in Modeling Earth Systems 11 (7), 2177–2213.

Volodin, E., Mortikov, E., Gritsun, A., Lykossov, V., Galin, V., Diansky, N., Gusev, A., Kostrykin, S., Iakovlev, N., Shestakova, A., Emelina, S., 2019. INM INM-CM5-0 model output prepared for CMIP6 CMIP.
URL `https://doi.org/10.22033/ESGF/CMIP6.1423`

Wang, Y., Heywood, K. J., Stevens, D. P., Damerell, G. M., 2021a. Seasonal extrema of sea surface temperature in CMIP6 models. Earth and Space Science Open Archive ESSOAr.

Wang, Y., Thomas, E. R., Hou, S., Huai, B., Wu, S., Sun, W., Qi, S., Ding, M., Zhang, Y., 2017. Snow accumulation variability over the West Antarctic Ice Sheet since 1900: A

comparison of ice core records with ERA-20C reanalysis. Geophysical Research Letters 44 (22), 11–482.

Wang, Y.-C., Hsu, H.-H., Chen, C.-A., Tseng, W.-L., Hsu, P.-C., Lin, C.-W., Chen, Y.-L., Jiang, L.-C., Lee, Y.-C., Liang, H.-C., et al., 2021b. Performance of the Taiwan Earth System Model in Simulating Climate Variability Compared with Observations and CMIP6 Model Simulations. Journal of Advances in Modeling Earth Systems, e2020MS002353.

Wille, J. D., Favier, V., Gorodetskaya, I. V., Agosta, C., Kittel, C., Beeman, J. C., Jourdain, N. C., Lenaerts, J. T., Codron, F., 2021. Antarctic atmospheric river climatology and precipitation impacts. Journal of Geophysical Research: Atmospheres 126 (8), e2020JD033788.

Wu, T., Zhang, F., Zhang, J., Jie, W., Zhang, Y., Wu, F., Li, L., Yan, J., Liu, X., Lu, X., et al., 2020. Beijing Climate Center Earth System Model version 1 (BCC-ESM1): model description and evaluation of aerosol simulations. Geoscientific Model Development 13 (3), 977–1005.

Wyser, K., Noije, T. v., Yang, S., Hardenberg, J. v., O'Donnell, D., Döscher, R., 2020. On the increased climate sensitivity in the EC-Earth model from CMIP5 to CMIP6. Geoscientific Model Development 13 (8), 3465–3474.

Yu, L., Yang, Q., Vihma, T., Jagovkina, S., Liu, J., Sun, Q., Li, Y., 2018. Features of extreme precipitation at Progress Station, Antarctica. Journal of Climate 31 (22), 9087–9105.

Yukimoto, S., Kawai, H., Koshiro, T., Oshima, N., Yoshida, K., Urakawa, S., Tsujino, H., Deushi, M., Tanaka, T., Hosaka, M., et al., 2019. The Meteorological Research Institute Earth System Model version 2.0, MRI-ESM2. 0: Description and basic evaluation of the physical component. Journal of the Meteorological Society of Japan. Ser. II.

Zhang, L., Delworth, T. L., Cooke, W., Yang, X., 2019. Natural variability of Southern

Ocean convection as a driver of observed climate trends. Nature Climate Change 9 (1), 59–65.

Ziehn, T., Chamberlain, M. A., Law, R. M., Lenton, A., Bodman, R. W., Dix, M., Stevens, L., Wang, Y.-P., Srbinovsky, J., 2020. The Australian Earth System Model: ACCESS-ESM1. 5. Journal of Southern Hemisphere Earth Systems Science 70 (1), 193–214.

Zwally, H. J., Li, J., Robbins, J. W., Saba, J. L., Yi, D., Brenner, A. C., 2015. Mass gains of the Antarctic ice sheet exceed losses. Journal of Glaciology 61 (230), 1019–1036.

Appendix

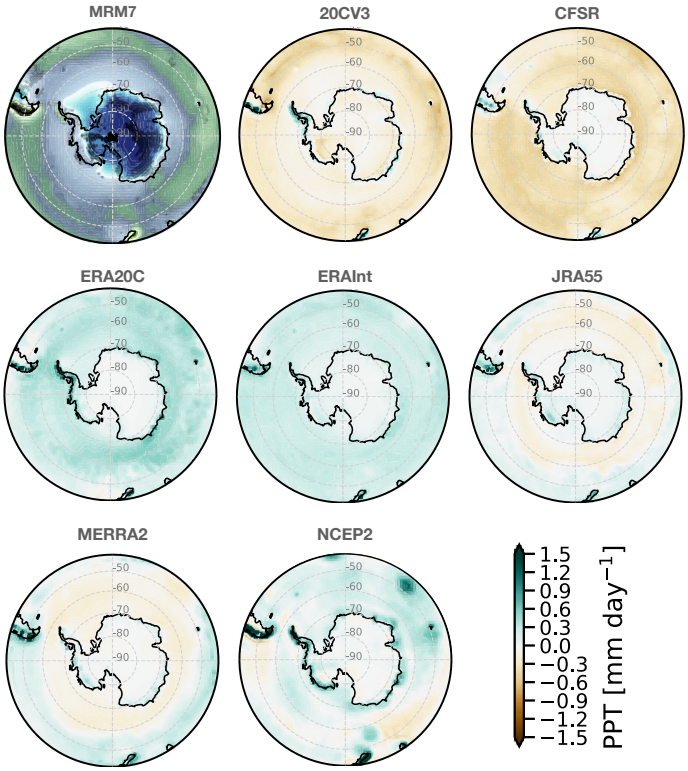

Figure A: Difference of each reanalysis' PPT mean-field from MRM7 (MRM7 - reanalysis), in mm day^{-1}. In the first panel (MRM7), shading represents the 1900-2014 mean-field of PPT, and stippling indicates the dataset's agreement within the interval $mean \pm 1STD$ ($\approx 86\%$ agreement).

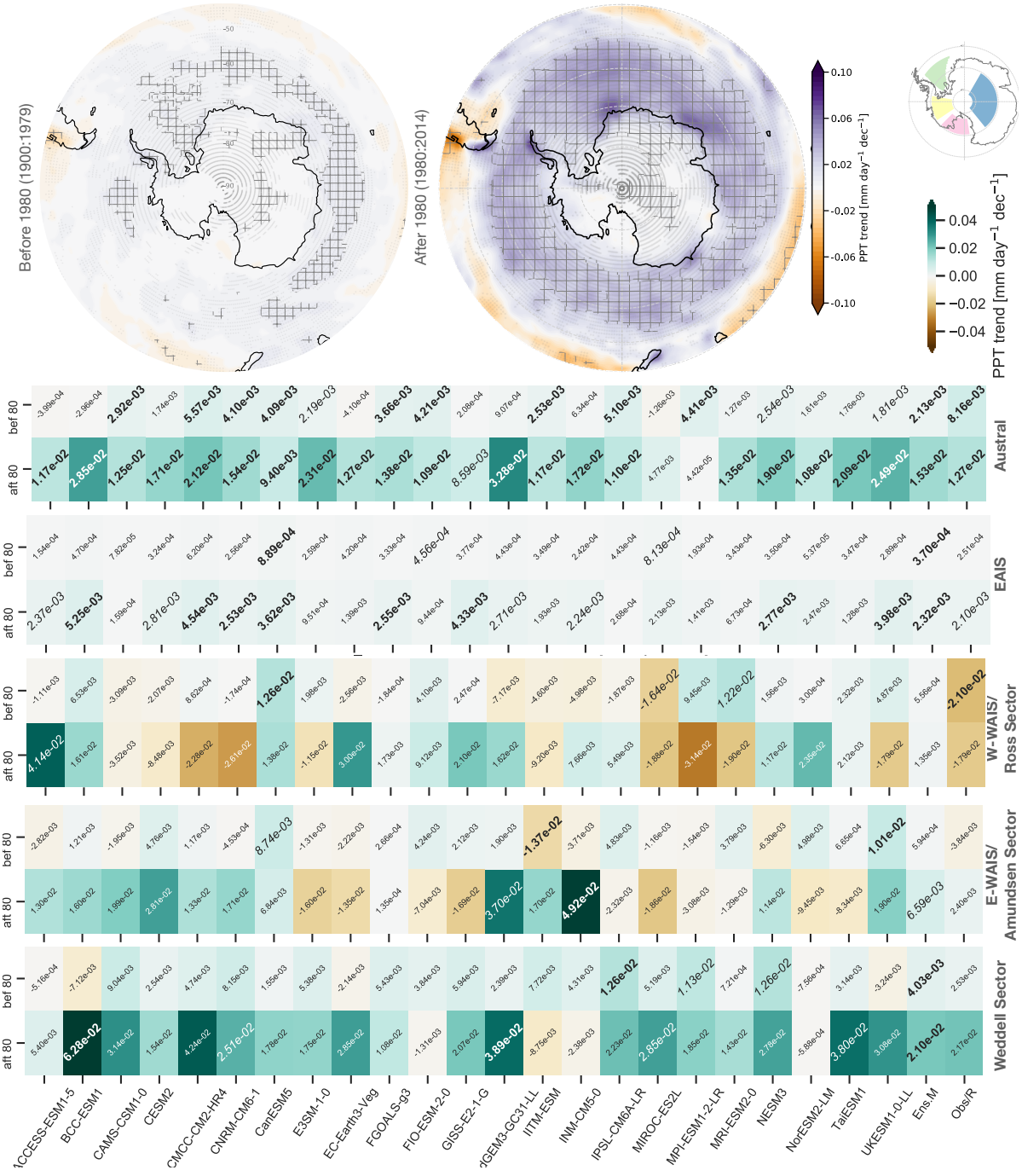

Figure B: Same as Figure 3.9, but detailing the PPT trends for each of the 23 CMIP models.

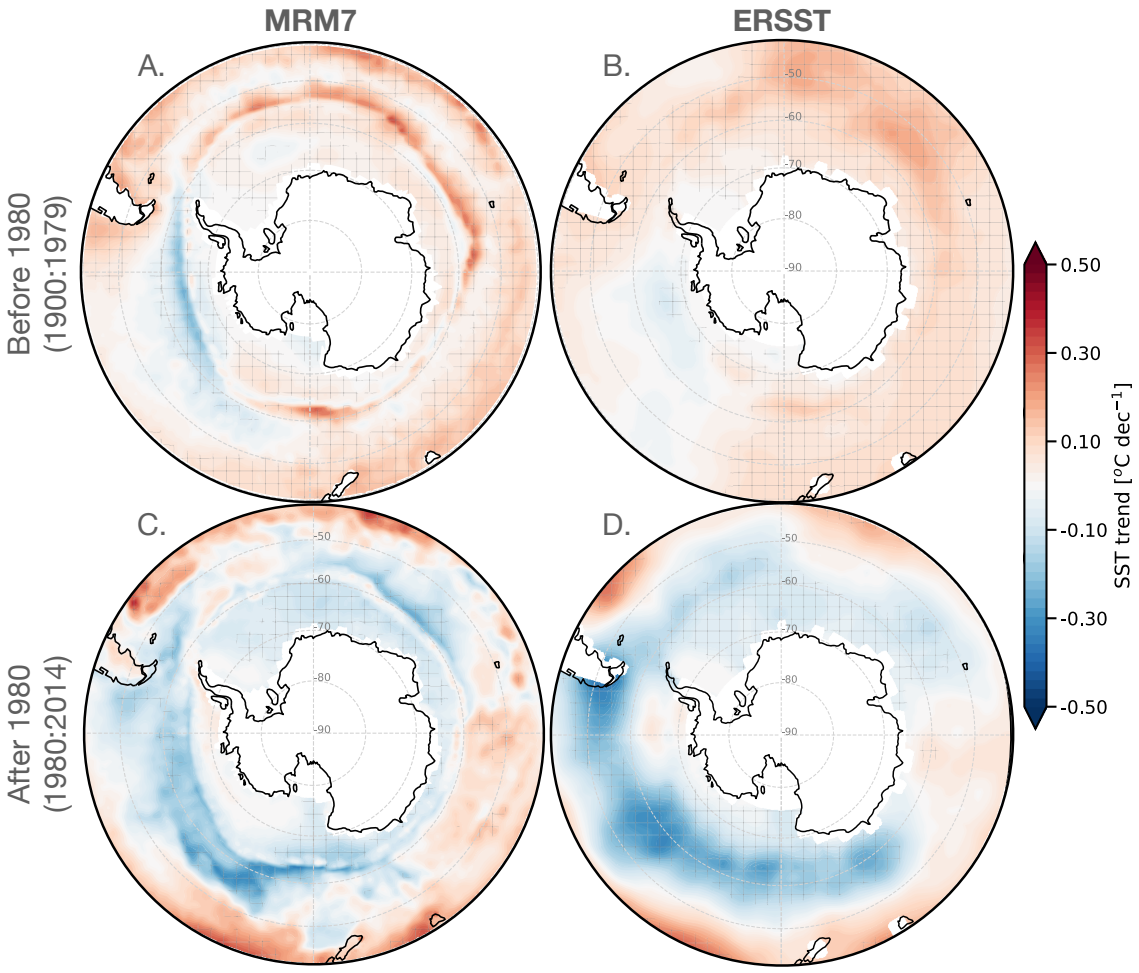

Figure C: Comparison between SST in MRM7 and in observations. The observational data is from NOAA's Extended Reconstructed Sea Surface Temperature (ERSST; Huang et al., 2017) v5 from 1854 to 2014. ERSSTv5 data is provided by the NOAA/OAR/ESRL PSL, Boulder, Colorado, USA, available on the Web site at `https://psl.noaa.gov/data/gridded/data.noaa.ersst.v5.html` (last access January 17, 2022)